Characteristics of Station-Derived Convective Cold Pools Over Equatorial Africa

Jannik Hoeller[1], Jan Olaf Haerter[1], and Nicolas A. Da Silva[1]

[1]Leibniz Centre for Tropical Marine Research

November 22, 2023

Abstract

Due to their potential role in organizing tropical mesoscale convective systems, a better understanding of cold pool (CP) dynamics in such regions is critical, particularly over land where the diurnal cycle further concentrates convective activity. Numerical models help disentangle the processes involved but often lack observational benchmark studies. To close this gap, we analyze nearly 43 years of five-minute resolution near-surface timeseries records from twelve automatic weather stations across equatorial Africa. We identify 4289 CPs based on criteria for temperature and wind. The identified CP gust fronts, which exhibit respective median temperature and specific humidity decreases of 5.2 K and 2.8 g/kg, closely correlate with satellite-observed brightness temperature discontinuities. Despite weak diurnal variation in precipitation, observed CP occurrence shows a pronounced diurnal cycle with an afternoon peak — a finding we attribute to low-level moisture conditions. Our findings can serve as observational benchmark to improve simulations of CP organization.

Characteristics of Station-Derived Convective Cold Pools Over Equatorial Africa

Jannik Hoeller[1,2], Jan O. Haerter[1,2,3,4], Nicolas Da Silva[1]

[1]Integrated Modeling, Leibniz Centre for Tropical Marine Research, Fahrenheitstr. 6, 28359 Bremen, Germany
[2]Niels Bohr Institute, Copenhagen University, Blegdamsvej 17, 2100 Copenhagen, Denmark
[3]Physics and Earth Sciences, Constructor University Bremen, Campus Ring 1, 28759 Bremen, Germany
[4]Department of Physics and Astronomy, University of Potsdam, Karl-Liebknecht-Straße 32, 14476 Potsdam, Germany

Key Points:

- 4289 cold pools are identified across equatorial Africa based on temperature and wind criteria.
- The occurrence and intensity of the observed cold pools are related to low-level moisture conditions and the depth of convection.
- The identified cold pool gust fronts closely correlate with satellite-observed brightness temperature discontinuities.

Corresponding author: Jannik Hoeller, `jannik.hoeller@leibniz-zmt.de`

Abstract

Due to their potential role in organizing tropical mesoscale convective systems, a better understanding of cold pool (CP) dynamics in such regions is critical, particularly over land where the diurnal cycle further concentrates convective activity. Numerical models help disentangle the processes involved but often lack observational benchmark studies. To close this gap, we analyze nearly 43 years of five-minute resolution near-surface timeseries records from twelve automatic weather stations across equatorial Africa. We identify 4289 CPs based on criteria for temperature and wind. The identified CP gust fronts, which exhibit respective median temperature and specific humidity decreases of $5.2\,K$ and $2.8\,g/kg$, closely correlate with satellite-observed brightness temperature discontinuities. Despite weak diurnal variation in precipitation, observed CP occurrence shows a pronounced diurnal cycle with an afternoon peak — a finding we attribute to low-level moisture conditions. Our findings can serve as observational benchmark to improve simulations of CP organization.

Plain Language Summary

Convective cold pools form when rain evaporates underneath thunderstorm clouds. The evaporation causes the air to cool and sink toward the ground, where it is deflected horizontally. Cold pools are thus associated with strong gusty winds, and over tropical land, they can be especially vigorous. Cold pools are also suggested to contribute to the organization of thunderstorm clouds into large clusters of rain-producing areas. The widespread, heavy rainfall can then cause flooding. To better predict such flooding in numerical weather models, having a precise observational basis for cold pool properties is essential — yet currently missing in equatorial Africa. We here provide such an observational benchmark by analyzing thousands of cold pools using timeseries of near-surface temperature, wind, humidity and precipitation. We additionally show that the cold pools can even be detected from satellite data when analyzing abrupt changes in cloud top temperature. Such satellite-based detection could open for cold pool studies across all tropical land areas — of great practical relevance to the prediction of thunderstorm clusters.

1 Introduction

Convective cold pools (CPs) are caused by the evaporation of rainfall beneath deep convective clouds (Zuidema et al., 2017). The resultant denser air volume within the subcloud layer spreads out laterally along the surface and is known to cause a so-called "gust front" along its edges. The gust front features strong horizontal and vertical winds along with moisture and temperature anomalies which together can give rise to additional deep convective events, e.g., under collisions (Purdom, 1976; Feng et al., 2015). CPs are thus important agents in mediating interactions between deep convective cells and thus the self-organization of thunderstorm systems (Simpson, 1980; Tompkins, 2001b; Haerter et al., 2019; Jensen et al., 2021).

Recent idealized cloud-resolving and large-eddy simulations have provided new quantitative and qualitative insight into CP structure and dynamics, such as scaling analysis to obtain a required mesh resolution (Fiévet et al., 2022), the potential origin of moisture rings (Langhans & Romps, 2015; Drager et al., 2020), and insight into interaction mechanisms (Tompkins, 2001a; Torri et al., 2015; Meyer & Haerter, 2020; Haerter et al., 2020). Such simulation studies have also triggered a range of simplified conceptual models, (Böing, 2016; Haerter, 2019; Haerter et al., 2019; Nissen & Haerter, 2021; Niehues et al., 2022), which may help elucidate some of the organizing mechanisms involved. New methods of CP detection in numerical studies have also been developed, which help automatize the tracking of CP gust fronts and their interactions in space and time (Gentine et al., 2016; Torri & Kuang, 2019; Fournier & Haerter, 2019; Henneberg et al., 2020; Hoeller et al., 2022; Hoeller, Fiévet, & Haerter, 2023).

Despite this progress in numerical and theoretical work, direct measurements of CPs are still limited to specific geographic regions, such as the tropical and sub-tropical ocean (Zipser, 1977; Zuidema et al., 2012; Vogel, 2017; Chandra et al., 2018; Vogel et al., 2021), and mid-latitude continental regions in Central Europe (Kirsch et al., 2021; Kruse et al., 2022) or North America (Mueller & Carbone, 1987; Wakimoto, 1982; Engerer et al., 2008; Hitchcock et al., 2019; van den Heever et al., 2021). With a focus on dust storms, in semi-arid tropical regions a CP detection method was suggested based on surface measurements and satellite microwave data (Redl et al., 2015).

The importance of collecting information on CPs and precipitation in deep tropical regions has been pointed out (Adams et al., 2015) but systematic, climatological studies on CPs in such regions are still rare or lacking. This may partially be due to difficult environmental conditions which pose challenging demands on equipment and maintenance (Parker et al., 2008). Also the availability of funds may hinder systematic long-term campaigns in some regions. A notable exception is the trans-African hydro-meteorological observatory (TAHMO) which offers a promising network of station measurements in many sub-Saharan African countries (van de Giesen et al., 2014). Using a range of stations from the TAHMO network, we here present a climatology of CP measurements for equatorial Africa and compare findings to previous work in other geographic regions.

2 Data

2.1 Station data

We utilize data from twelve ATMOS41 automatic weather stations (AWS) in equatorial Africa (Fig. 1), operated by TAHMO (TAHMO, 2023). The stations are situated in Cameroon, the Democratic Republic of the Congo (DR Congo), Nigeria, and Uganda. In order to investigate the influence of regional climatic differences on CPs, we group stations according to their respective deployment countries in the following analysis.

The AWS provide data at a temporal resolution of five minutes. All stations are installed at an approximate height of two meters above the surface. For our analysis, we employ the station records of precipitation, atmospheric pressure, air temperature, relative humidity, and wind gust speed. To derive the wind gust speed, the ATMOS41 measures the instantaneous wind speed every ten seconds and outputs the maximum instantaneous wind speed value within the corresponding five-minute interval as wind gust speed. If an instantaneous wind speed is larger than eight times the running average of the previous ten instantaneous measurements, the measurement is rejected. While this method may prevent spurious spikes in the wind record under normal conditions, it can cause missing wind data in cases of large and sudden wind changes. Given the frequent occurrence of such strong wind variations associated with CP gust fronts, approximately 22% of all identified CPs have an incomplete wind record.

We analyze the data recorded by the stations from January 1, 2019, to September 30, 2023. As not all stations were operational throughout the entire period, we limit our analysis for each station to days with complete air temperature record. Additionally, we require the air temperature to be recorded for a minimum of ten consecutive minutes from the previous day and for the subsequent 120 minutes on the following day. The resulting number of analysis days per station is indicated in Fig. 1. In total, we analyzed 15602 days and thus nearly 43 years of station data.

Based on the station-measured variables, we additionally compute both mixing ratio, r and saturated mixing ratio, r_{sat} (see Text S1), and derive the mixing ratio deficit, $r_D \equiv r_{sat} - r$ and the specific humidity, $q \equiv r/(1 + r)$.

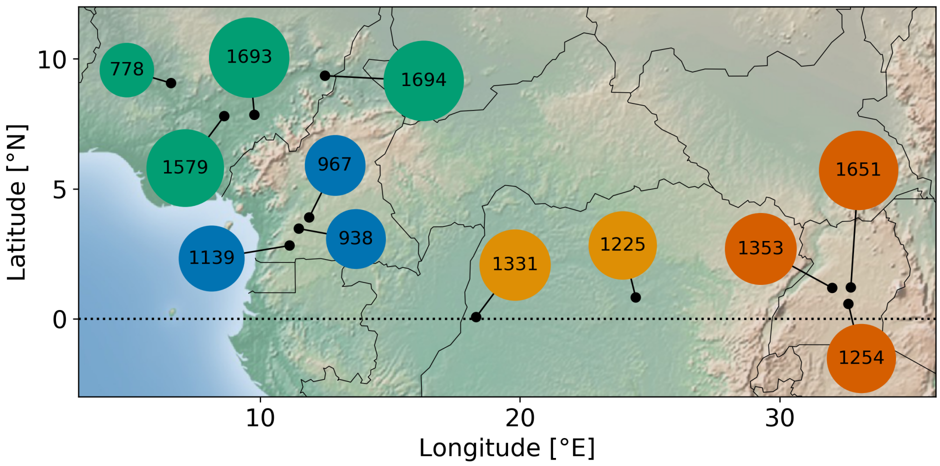

Figure 1: **Employed weather station data.** Map of equatorial Africa with station locations (filled black circles) utilized in this study. Numbers represent available days of station data with a complete record of air temperature, T. The stations are grouped into four regions denoted by the colored circles: Cameroon (blue), Democratic Republic of the Congo (yellow), Nigeria (green), Uganda (red). The area of colored circles is proportional to the available days of station data.

2.2 Satellite data

Apart from the station data, we utilize infrared brightness temperature measurements which we derive from satellite-measured effective radiances. The radiances are extracted from Meteosat Second Generation (MSG) 0° products provided by the European Organisation for the Exploitation of Meteorological Satellites (EUMETSAT) (EUMETSAT, 2023). The data has a baseline repeat cycle of $15\,min$ and a spatial resolution of $3\,km$ in the sub-satellite point. To convert the radiances to brightness temperatures we employ equation 5.3 and the corresponding regression coefficients of EUMETSAT (2012).

3 Methods

3.1 Cold Pool Detection Algorithm

(i) Temperature criterion. A potential CP event is detected at a given time t if three conditions apply: similar to Kirsch et al. (2021) we require a substantial temperature decrease $\Delta T \leq -2\,K$, within the $20\,min$ window from $t - 5\,min$ to $t + 15\,min$. Additionally, we require the decrease of ΔT to be monotonic and $T(t) - T(t - 5\,min) \leq 0.5\,K$.

(ii) Wind criterion. To verify detected potential CP events, we adapt the wind criterion introduced by Kruse et al. (2022). For this purpose, we compute the wind gust anomaly for each time t as

$$\Delta u_g(t) \equiv u_g(t) - \overline{u}_g(t)\,, \tag{1}$$

where u_g is the wind gust speed and $\overline{u}_g$ its centered 2-hour running mean, i.e., the mean value of the 25 wind gust speeds recorded during the the corresponding 2-hour window.

For a potential CP event at time t we identify the maximum wind gust anomaly, Δu_g^{max}, between $t - 20\,min$ and $t + 40\,min$. We consider it as CP event if

$$\Delta u_g^{max} \geq \overline{\Delta u}_g(t) + 3\,\sigma_{\Delta u_g}(t)\,, \tag{2}$$

with the centered 24-hour running mean of the wind gust anomaly, $\overline{\Delta u_g}$, and the corresponding 24-hour running standard deviation, $\sigma_{\Delta u_g}$.

As the CP onset is defined based on the temperature criterion, we also search for associated wind gusts in a $20\,min$ time window before CP onset. We choose $20\,min$ rather than the $10\,min$ used by Kruse et al. (2022) since our temperature criterion involves a minimum decrease of $-0.5\,K$ within $5\,min$ to define the onset of potential CPs and might thus delay the onset in comparison to Kruse et al. (2022). The $40\,min$ time window after CP onset allows significant wind offsets while ensuring a temporal relation between ΔT and Δu_g^{max}.

In case of missing wind gust anomalies between $t{-}20\,min$ and $t{+}40\,min$, we identify the maximum wind gust, u_g^{max} within this time window rather than Δu_g^{max} and consider the event a CP if

$$u_g^{max} \geq \overline{u}_g(t-80\,min) + 2\,\sigma_{u_g}(t-80\,min)\,. \tag{3}$$

By evaluating the centered 2-hour running mean $\overline{u}_g$ and the corresponding standard deviation, σ_{u_g}, $80\,min$ before CP onset, we keep again a $20\,min$ offset between CP onset and the 2-hour time window of the reference values. If no wind gust data has been recorded between $t-20\,min$ and $t+40\,min$, or if the reference values $\overline{u}_g(t-80\,min)$ and $\overline{u}_g(t{-}80\,min)$ could not be computed due to missing data, we consider the event as "no CP."

Differing from Kruse et al. (2022), we evaluate the wind criterion based on wind gust rather than wind speed. Since we work with station data with a temporal resolution of $5\,min$ in contrast to $1\,min$ in (Kruse et al., 2022), we find wind gust a better indicator for CP gust fronts than wind speed.

(iii) Duplicate detection check. Often, a CP fulfills the defined criteria (i) and (ii) not only at time t, but also at subsequent time steps. Depending on the evolution of temperature and wind gust behind the CP gust front, time steps in which the criteria are met can even be separated from each other by time steps in which the criteria are not met. In order to avoid duplicate detection of a given CP, we drop detected CP events if at least one other CP event was detected within $20\,min$ before that particular event. Given the variety of environmental conditions under which we observe CPs at our station locations, we find this definition to be more permissive than the absolute $60\,min$ time window after detected temperature decreases, within which Kirsch et al. (2021) consider any detected decrease as part of the same event.

3.2 Determination of Cold Pool Anomalies

We analyze the effects of a detected CP with respect to different station-measured meteorological variables by considering a time window relative to CP onset, t_0, from $t_0{-}40\,min$ to $t_0{+}120\,min$. Within this time window, we evaluate the CP associated anomalies $y'(t) \equiv y(t) - y_{ref}$ for a meteorological variable y based on an unperturbed reference state y_{ref}, which we define as the temporal mean of instantaneous measurements in a time interval before CP onset. Since the onset is defined based on the temperature drop and thus could be different for other variables, we choose the time interval from $t_0{-}40\,min$ to $t_0{-}20\,min$ to keep a sufficient margin of $20\,min$ to the CP onset while preserving the required temporal proximity. To minimize any distortion of the reference state through the diurnal cycle, we deviate from this definition only for temperature anomalies and follow the approach of the refined temperature drop from Kruse et al. (2022) instead, i.e., we consider the maximum temperature of the two measurements in the $10\,min$ time window preceding the CP onset as unperturbed reference temperature.

Due to the coarser temporal resolution, we extend the time window in which we analyze the anomalies before CP onset to $60\,min$ for satellite-measured $10.8\,\mu m$ brightness temperatures, $BT_{10.8}$, and define the reference brightness temperature, $BT_{10.8}^{ref}$, as the mean of the three observations in the time interval from $t_0 - 60\,min$ to $t_0 - 30\,min$. As there might not be a brightness temperature observation at the station-derived CP onset, t_0, we define the closest satellite time step as $\hat{t}_0$ and measure the CP time relative to it. The brightness temperature anomalies, $BT'_{10.8}$, are then computed analogously to those for station-measured variables. Moreover, to further investigate the space-borne CP signature, we additionally determine the temporal change of $BT'_{10.8}$, as $\Delta BT'_{10.8}(t) = BT'_{10.8}(t) - BT'_{10.8}(t - 15\,min)$.

4 Results

4.1 Seasonal and Diurnal Cycle of Observed Cold Pools

First, we derive the seasonal and diurnal cycles of CPs in the different sub-regions (Fig. 1) and relate them with precipitation, convection depth and moisture conditions (Fig. 2). With about 0.3–0.6 CPs per day in the high seasons (Fig. 2a, Table S2), equatorial Africa is a region with particular CP abundance compared to previous climatologies in other continental regions (Redl et al., 2015; Kirsch et al., 2021; Kruse et al., 2022). In every sub-region, the number of CPs peaks twice during the course of the year with a first maximum between March and May and a second maximum between September and October. The bi-modality in the annual cycle of CPs largely corresponds to the latitudinal migration of the Inter-Tropical Convergence Zone (ITCZ) which is reflected in the precipitation seasonal cycles (Fig. 2c). However, we note that precipitation may not explain all the features of the annual cycle of CPs and the differences between sub-regions. For instance, Nigeria presents a single precipitation peak in September whereas the occurrence of CPs peaks in both May and September. There, the strong CP activity during May may be related to the combination of deeper convection (Fig. 2e) fed by high equivalent potential temperatures (θ_E; Fig. S1) and of higher low-level water vapor mixing ratio deficit (r_D; Fig. 2g) boosting rain evaporation. We also note that Uganda receives the least precipitation among sub-regions while experiencing the most of CPs during the year. We attribute the larger number of CPs in Uganda to generally drier conditions at low levels (Fig. 2g).

The diurnal cycle of CPs strongly peaks between 15 LT and 18 LT in most of the regions with the exception of Nigeria where the peak is reached between 18 LT and 21 LT (Fig. 2b). The high CP activity during the afternoon can be directly related to the afternoon peak in (deep) convection, highlighted by maxima in precipitation (Fig. 2d) and lower brightness temperatures (Fig. 2f). Consistently with earlier studies (Zhang et al., 2016; Camberlin et al., 2018; Andrews et al., 2023), precipitation shows secondary nocturnal peaks in Uganda and Congo, and remains high during the night in Nigeria, whereas the proportion of CPs displays local minima during these hours. This mismatch between precipitation and CPs is likely to be related to both the decline of convection during the night (leading to weaker rainfall intensities and downdrafts) and to moister conditions at the surface (reducing rainfall evaporative cooling; Fig. 2h) which both inhibit CP formation (Zuidema et al., 2017).

4.2 Observed Cold Pool Characteristics

We further characterize equatorial African CPs by examining their related temperature and moisture anomalies (defined in Sec. 3.2). On average, a CP in equatorial Africa is accompanied by a $5\,K$ drop in temperature (compared to $3\,K$ in Germany; Kirsch et al. (2021)) occurring in about 30 minutes, with little variability among sub-regions (Fig. 3a, Table S2). Different from Kirsch et al. (2021) over Germany, we generally observe a decrease in specific humidity after the passage of CPs over equatorial Africa (Fig. 3d). Interestingly, we find that the magnitude of this decrease is smaller in the elevated (Table S1) stations of Uganda ($-1\,g/kg$) characterized by less deep convection (Fig. 2e,f)

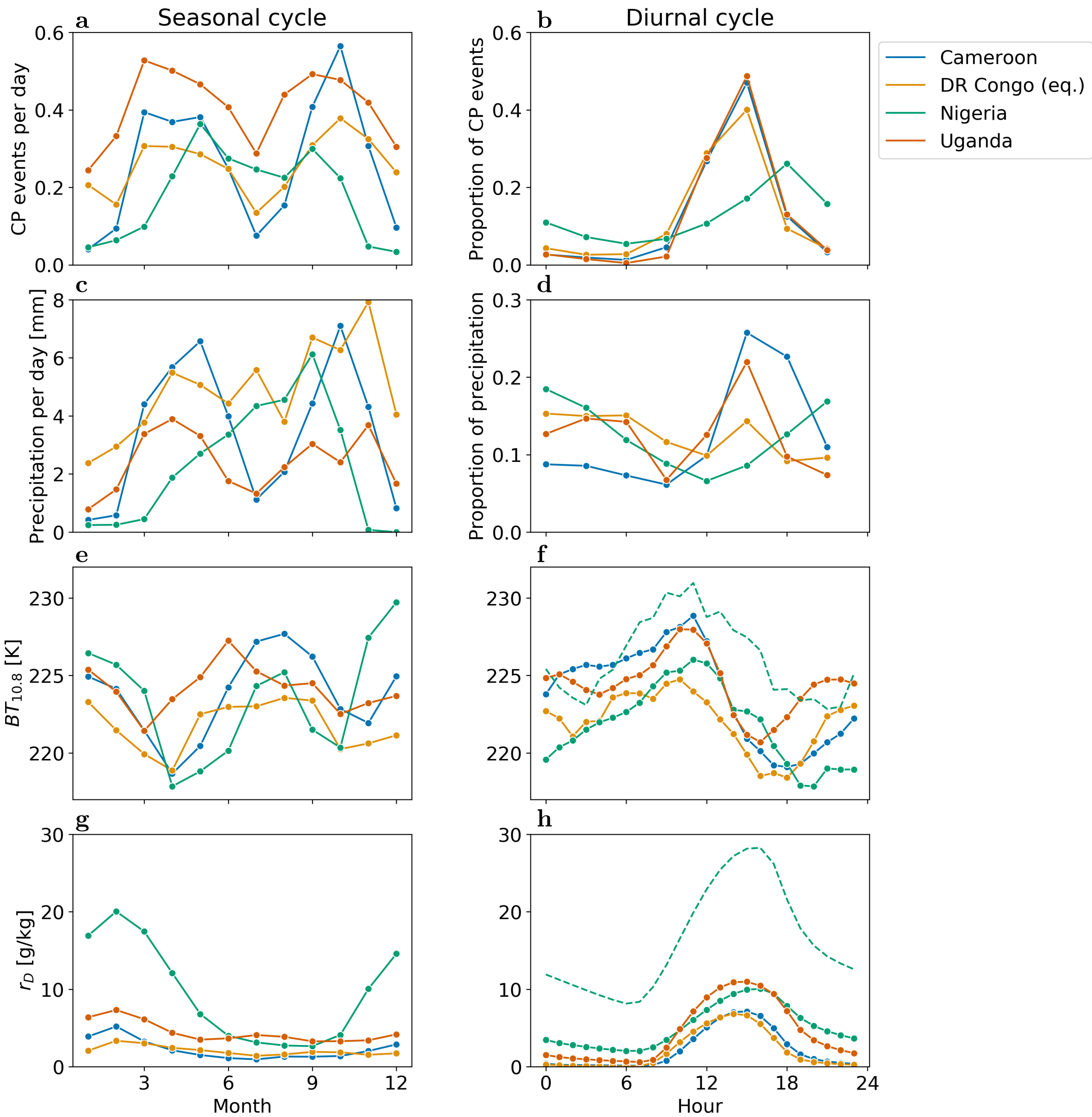

Figure 2: **Observed seasonal and diurnal cycles.** **a**, Mean number of daily cold pool (CP) events for each month. Lines interpolate linearly between markers to facilitate the interpretation; colors indicate different regions. The number of CP events is normalized based on the number of analyzed days per month and region. **b**, Proportion of CP events at different times of the day. Each marker represents the proportion of CP events observed within a given 3-hour time interval, starting with the interval [0,3) for the marker at 0 LT. Lines and colors analogous to (a). **c**, Analogous to (a) but for precipitation. **d**, Analogous to (b) but for precipitation. **e**, Mean 10.8 μm brightness temperature, $BT_{10.8}$, of deep clouds ($BT_{10.8} \leq 240\,K$) for each month. Lines and colors analogous to (a). **f**, Mean $BT_{10.8}$ of deep clouds at different times of the day. Intervals, lines and colors analogous to (b). The two lines for Nigeria represent rainy months (Apr–Oct, solid line with markers) and dry months (Nov–Mar, dashed). **g**, Analogous to (e) but for mean mixing ratio deficit, r_D. **h**, Analogous to (f) but for mean r_D.

and drier low-level environments (Fig. 2g,h) compared to the other sub-regions (about $-3\,g/kg$). Less deep convection is likely to be associated with less elevated (relative to the surface level) convective downdrafts (Zuidema et al., 2017) importing less upper-level dry air to the surface, which combined with enhanced rain evaporation due to drier environments, may explain the reduced decline in specific humidity over Uganda. When considering the 25% driest (moistest) low-level pre-CP environments, we further evidence the large impact of moisture conditions, and thus of rain evaporation, on CP temperature and moisture anomalies in all sub-regions (Fig. 2b,c,e,f). Indeed, we find CP anomalies that are on average $3\,K$ cooler and $2\,g/kg$ moister in the driest pre-CP conditions than in the moistest pre-CP conditions. We note weak maxima in specific humidity occurring few minutes after the CP onset (so-called moisture rings) over Cameroon, Uganda and Congo for the driest pre-CP environments. Finally, the temporal evolutions of r_D (Fig. 3g,h,i) reveal that in the driest environments, rain evaporation is not sufficient to saturate the low-level air (similar to Germany; Kirsch et al. (2021)).

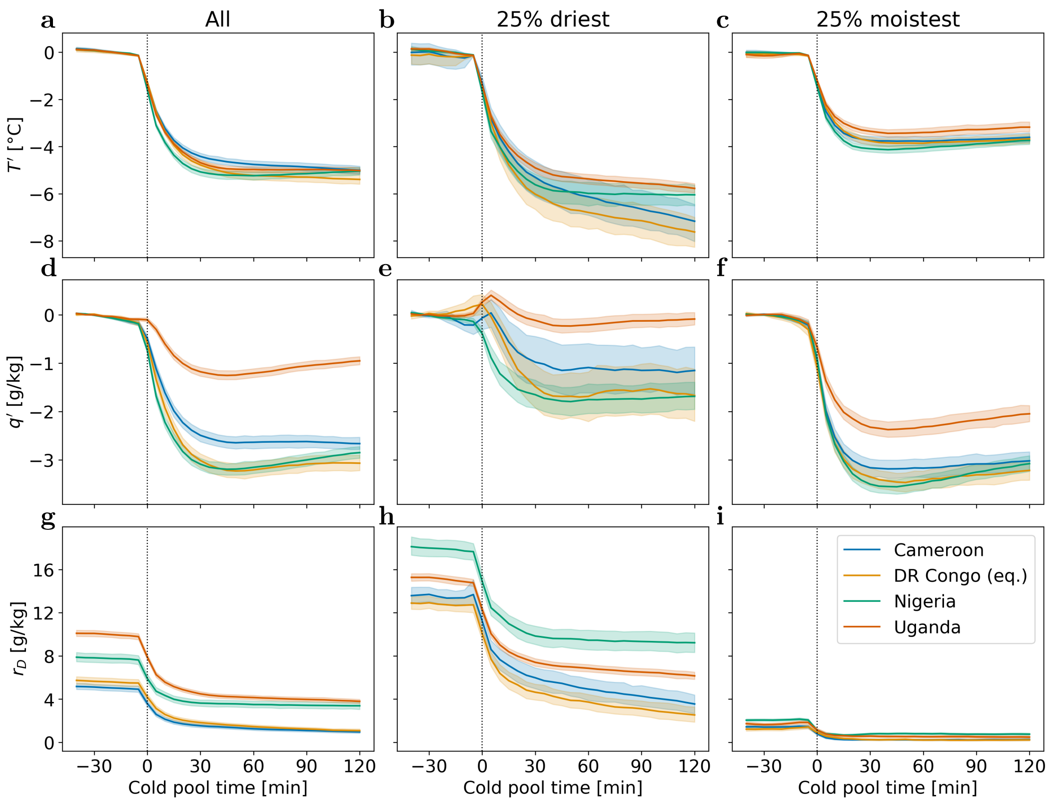

Figure 3: **Station-derived cold pool (CP) properties relative to CP onset, t_0.** **a**, Mean temperature anomalies, T', for different regions; shading indicates the 95% confidence interval. **b**, Analogous to (a) but for the 25% driest CPs of each region w.r.t. the reference mixing ratio deficit, r_D^{ref}, prior to t_0. **c**, Analogous to (b) but for the 25% moistest CPs. **d–f**, Analogous to (a)–(c) but for mean specific humidity anomalies, q'. **g–i**, Analogous to (a)–(c) but for mean mixing ratio deficits, r_D. Note that only timeseries of CPs, where t_0 is more than 120 minutes apart from other CP onsets, are included in the analysis.

Moving to CP cloud characteristics, we find that 92% (Nigeria) to 100% (Congo) of CP gust fronts are accompanied by shallow or deep convective clouds (Fig. S2a). More specifically, a CP is generally accompanied by a strong (reaching $30\,K$ in Cameroon) decrease in $BT_{10.8}$ (Fig. 4a). The $BT_{10.8}$ minimum is typically reached 30–45 minutes after CP onset. While this minimum is delayed w.r.t. the CP onset, we find a minimum of the time derivative of $BT'_{10.8}$ synchronized with the CP onset in all sub-regions (Fig. 4b). This observation suggests that CPs in equatorial Africa, and potentially other regions, might be detectable from space-borne satellite data.

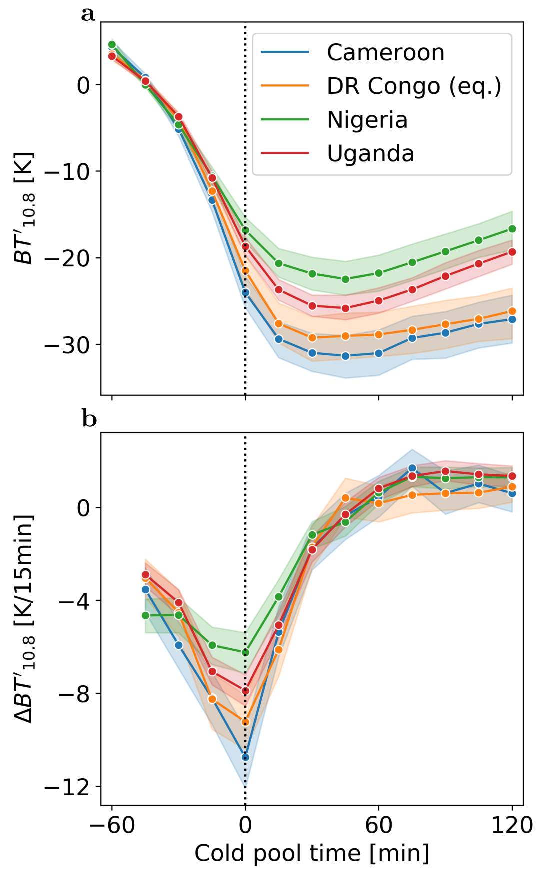

Figure 4: **Space-borne signatures of cold pools (CPs) relative to CP onset, $\hat{t}_0$.** **a**, Mean 10.8μm brightness temperature anomalies, $BT'_{10.8}$, of station-derived CPs for different regions; shading indicates the 95% confidence interval. **b**, Analogous to (a) but for the corresponding derivative $\Delta BT'_{10.8}$.

4.3 Cold Pool Examples With Deep and Shallow Convection

We now turn to two contrasting examples of observed CPs (Fig. 5). The two station locations at which the CPs were detected are indicated in Fig. 5a).

The first CP (Fig. 5; left column) was detected in DR Congo at station TA673 on November 28, 2021, at 13:40 UTC. The CP was associated with a mesoscale convective system, visible in the satellite-derived 10.8 μm brightness temperature image at 13:45 UTC (Fig. 5b). The corresponding brightness temperature timeseries of different satellite channels at the station are depicted in Fig. 5d). All channels show a significant brightness temperature decrease around CP onset, with a maximum decrease rate right at the onset. Between 12:30 and 14:45 UTC, the brightness temperature dropped by 85 K in the 10.8 μm channel and then slowly increased again. The station record (Fig. 5f) further reveals a massive air temperature drop of 9.6 K between 13:40 and 14:00 UTC, accompanied by increased wind gust speeds of up to 6.5 m/s. By 14:00 UTC, when the temperature stabilized again, the air became fully saturated. Five minutes later, the rainfall intensity peaked at approximately 65 mm/h.

The second CP (Fig. 5; right column) was detected in Uganda at station TA222 on July 2, 2021, at 12:05 UTC. During the time it was detected, the CP featured arc-shaped shallow convection at the gust front, distinctly separated from the parent convection by clear skies (Fig. 5c). The corresponding brightness temperature timeseries at the station (Fig. 5e) confirm the passage of low-level clouds right at the time of the station-derived CP onset. Around the CP onset, no rainfall was measured at the station (Fig. 5g). This time, the observed wind gust speeds increase approximately 5–10 minutes before the drop in air temperature and reach a peak value of 10 m/s at CP onset.

5 Summary and Discussion

The present study provides multi-year statistics of cold pool characteristics in equatorial Africa, based on five-minute near-surface weather data. Using detection methods similar to those in previous studies focused on mid-latitude continental regions, key findings include that temperature drops upon gust front passage often exceed 5 K and specific humidities typically decrease by more than 3 g/kg. Weak moisture rings can only be identified for the driest cold pools in some of the regions — in agreement with Kruse et al. (2022) for data in the Netherlands where moisture rings were generally not detected.

Seasonally, the rate of cold pool occurrence roughly follows precipitation statistics. Yet, diurnally, the fact that the nocturnal boundary layer is often close to saturation may focus the diurnal cycle of cold pool occurrence on the drier late afternoon times. This may have important implications for thunderstorm organization through cold pool activity: the limited time window where cold pools actually occur during the day means that self-organization may be limited to relatively short periods of the day. One could speculate that it is the lack of cold pool activity that limits the duration of mesoscale convective systems, often less than 12 hours, rather than the precipitation itself (which is more spread out over the day). Future studies should analyze if deep convection is more scattered during the nocturnal periods when fewer cold pools occur. Comparisons with oceanic cold pools and their organizational effects, which tend to be weaker (Zuidema et al., 2017), would be useful.

Our cold pool detection algorithm can be adapted to other regions, provided that there are in-situ weather stations measuring surface wind and temperature with at least a 5-minute temporal resolution. However, in-situ weather stations meeting this requirement are still limited in the tropics, whereas cold pools are abundant. Encouragingly, our findings may have implications for satellite-based cold pool detection: we show that the gust front passage clearly correlates with discontinuities in satellite-derived brightness temperature. We generally observe a significant decrease in brightness temperatures around the time of the gust front passage, with maximum decrease rates at the station-derived cold pool onset. Our findings thus suggest that cold pools in equatorial Africa, and potentially other regions, could be directly detectable from geostationary satellite data on a continental scale. Even in cases where not all parts of a cold pool gust front exhibit brightness temperature drops (Fig. S2b), neural networks, such as those developed by Hoeller, Fiévet, and Haerter (2023), may still possess the capability to detect the overall two-dimensional pattern and accurately track the gust front.

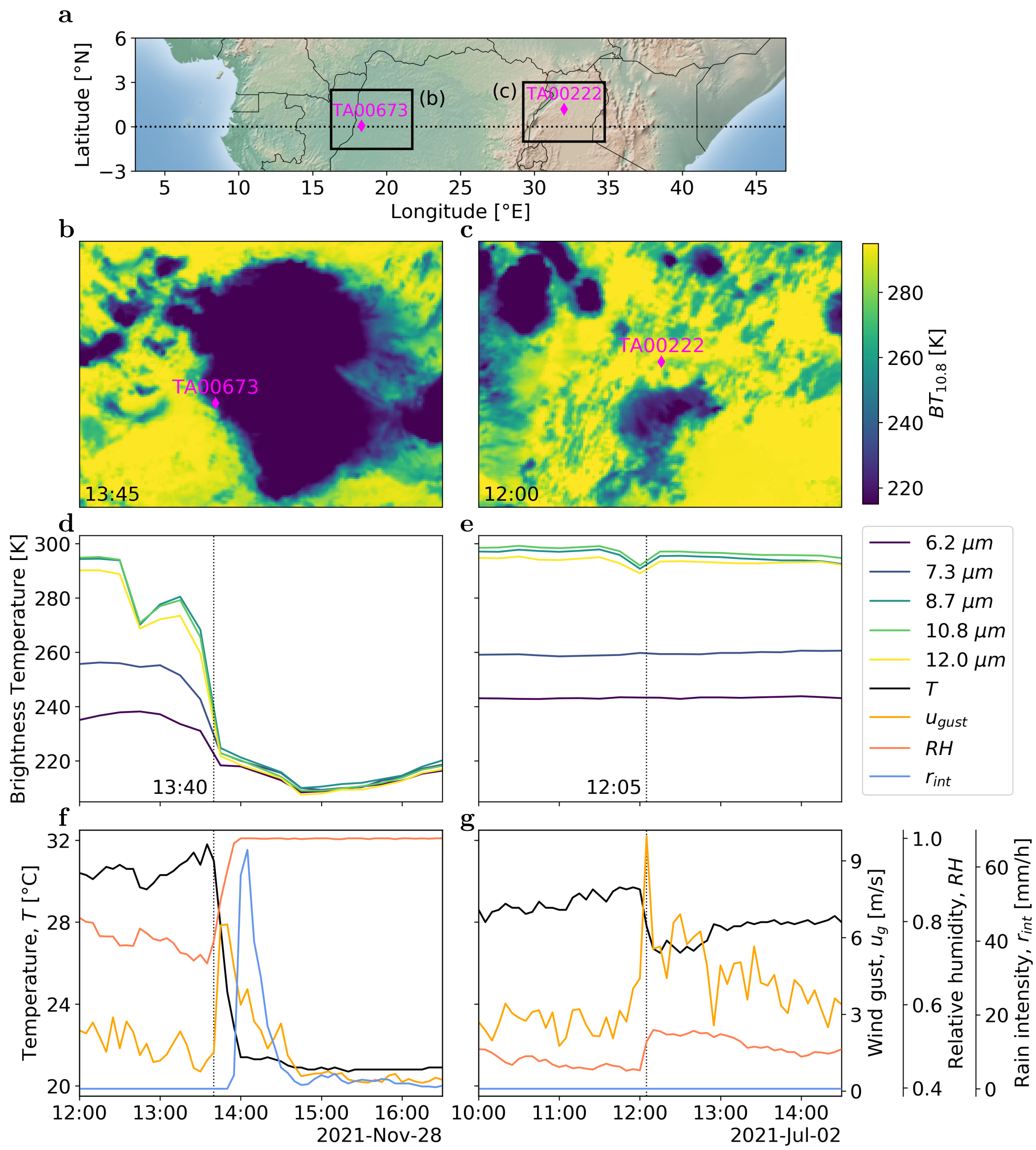

Figure 5: **Cold pool (CP) case studies. a**, Map displaying the locations of the stations utilized in the two case studies. Rectangles indicate the regions depicted in (b) and (c). **b**, Satellite-derived 10.8μm brightness temperatures, $BT_{10.8}$, in the vicinity of station TA00673 on November 28, 2021, at 13:45, close to a station-derived CP onset at 13:40. **c**, Analogous to (b) but for station TA00222 on July 2, 2021, at 12:00 and a CP onset at 12:05. **d**, Timeseries of satellite-derived brightness temperatures at station TA673 during the CP event visualized in (b). **e**, Analogous to (d) but for the CP event at station TA222 visualized in (c). **f-g**, Analogous to (d-e) but for different near-surface observations.

Data Availability Statement

Both the code for the cold pool gust front identification and the processed data sets are licensed under Creative Commons Attribution 4.0 International and were used in version 1.0 (Hoeller, Haerter, & Silva, 2023). The raw data of the automatic weather stations was provided by TAHMO (TAHMO, 2023) and is not publicly available. Interested parties may contact info@tahmo.org for this data. The satellite-observed radiances were extracted from Meteosat Second Generation (MSG) 0° products, provided by EUMETSAT without a licence on an unrestricted basis (EUMETSAT, 2023). Figures were made with Matplotlib version 3.5.2 (Hunter, 2007; Caswell et al., 2022) and seaborn version 0.12.2 (Waskom, 2021).

Conflicts of Interest Statement

The authors have no conflicts of interest to declare.

Acknowledgments
The authors gratefully acknowledge funding by a grant from the VILLUM Foundation (grant number: 13168) and the European Research Council (ERC) under the European Union's Horizon 2020 research and innovation program (grant number: 771859) and the Novo Nordisk Foundation Interdisciplinary Synergy Program (grant no. NNF19OC0057374). This work used resources of the Deutsches Klimarechenzentrum (DKRZ), granted by its Scientific Steering Committee (WLA) under project ID bb1166. Additionally, the authors thank the Trans-African Hydro-Meteorological Observatory (TAHMO) for the provision of meteorological data. Interested parties may contact info@tahmo.org for these data.

References

Adams, D. K., Fernandes, R. M., Holub, K. L., Gutman, S. I., Barbosa, H. M., Machado, L. A., ... others (2015). The amazon dense gnss meteorological network: A new approach for examining water vapor and deep convection interactions in the tropics. *Bulletin of the American Meteorological Society*, *96*(12), 2151–2165.

Andrews, P. C., Cook, K. H., & Vizy, E. K. (2023). Mesoscale convective systems in the congo basin: seasonality, regionality, and diurnal cycles. *Climate Dynamics*, 1–22. doi: 10.1007/s00382-023-06903-7

Böing, S. J. (2016). An object-based model for convective cold pool dynamics. *Mathematics of Climate and Weather Forecasting*, *2*(1).

Camberlin, P., Gitau, W., Planchon, O., Dubreuil, V., Funatsu, B. M., & Philippon, N. (2018). Major role of water bodies on diurnal precipitation regimes in eastern africa. *International Journal of Climatology*, *38*(2), 613-629. Retrieved from `https://rmets.onlinelibrary.wiley.com/doi/abs/10.1002/joc.5197` doi: https://doi.org/10.1002/joc.5197

Caswell, T. A., Droettboom, M., Lee, A., de Andrade, E. S., Hoffmann, T., Klymak, J., ... Ivanov, P. (2022). *matplotlib/matplotlib: Release (version 3.5.2) [software].* Zenodo. Retrieved from `https://doi.org/10.5281/zenodo.6513224` doi: 10.5281/zenodo.6513224

Chandra, A. S., Zuidema, P., Krueger, S., Kochanski, A., de Szoeke, S. P., & Zhang, J. (2018). Moisture distributions in tropical cold pools from equatorial indian ocean observations and cloud-resolving simulations. *Journal of Geophysical Research: Atmospheres*, *123*(20), 11–445.

Drager, A. J., Grant, L. D., & van den Heever, S. C. (2020). Cold pool responses to changes in soil moisture. *Journal of Advances in Modeling Earth Systems*, *12*(8), e2019MS001922.

Engerer, N. A., Stensrud, D. J., & Coniglio, M. C. (2008). Surface characteristics of observed cold pools. *Monthly Weather Review*, *136*(12), 4839–4849.

EUMETSAT. (2012). *The conversion from effective radiances to equivalent brightness temperatures (version 1).* Retrieved from `https://www-cdn.eumetsat.int/files/2020-04/pdf_effect_rad_to_brightness.pdf`

EUMETSAT. (2023). *Meteosat second generation (msg) high rate seviri level 1.5 image data - 0 degree [dataset].* Retrieved from `https://navigator.eumetsat.int/product/EO:EUM:DAT:MSG:HRSEVIRI`

Feng, Z., Hagos, S., Rowe, A. K., Burleyson, C. D., Martini, M. N., & de Szoeke, S. P. (2015). Mechanisms of convective cloud organization by cold pools over tropical warm ocean during the amie/dynamo field campaign. *Journal of Advances in Modeling Earth Systems*, *7*(2), 357–381.

Fiévet, R., Meyer, B., & Haerter, J. O. (2022). On the sensitivity of convective cold pools to mesh resolution. *Earth and Space Science Open Archive*, 24. Retrieved from `https://doi.org/10.1002/essoar.10512297.1` doi: 10.1002/essoar.10512297.1

Fournier, M. B., & Haerter, J. O. (2019). Tracking the gust fronts of convective cold pools. *Journal of Geophysical Research: Atmospheres*, *124*(21), 11103–11117.

Gentine, P., Garelli, A., Park, S., Nie, J., Torri, G., & Kuang, Z. (2016). Role of surface heat fluxes underneath cold pools. *Geophys. Res. Lett.*, *43*, 874-883. doi: 10.1002/2015gl067262

Haerter, J. O. (2019). Convective self-aggregation as a cold pool-driven critical phenomenon. *Geophysical Research Letters*, *46*(7), 4017–4028. doi: https://doi.org/10.1029/2018GL081817

Haerter, J. O., Böing, S. J., Henneberg, O., & Nissen, S. B. (2019). Circling in on convective organization. *Geophysical Research Letters*, *46*(12), 7024–7034. doi: https://doi.org/10.1029/2019GL082092

Haerter, J. O., Meyer, B., & Nissen, S. B. (2020). Diurnal self-aggregation. *npj Climate and Atmospheric Science*, *3*. doi: 10.1038/s41612-020-00132-z

Henneberg, O., Meyer, B., & Haerter, J. O. (2020). Particle-based tracking of cold pool gust fronts. *J. Adv. Model. Earth Syst.*, *12*. doi: 10.1029/2019ms001910

Hitchcock, S. M., Schumacher, R. S., Herman, G. R., Coniglio, M. C., Parker, M. D., & Ziegler, C. L. (2019). Evolution of pre-and postconvective environmental profiles from mesoscale convective systems during pecan. *Monthly Weather Review*, *147*(7), 2329–2354.

Hoeller, J., Fiévet, R., & Haerter, J. O. (2022). U-net segmentation for the detection of convective cold pools from cloud and rainfall fields. *Authorea Preprints*.

Hoeller, J., Fiévet, R., & Haerter, J. O. (2023). Detecting cold pool family trees in convection resolving simulations. *Authorea Preprints*.

Hoeller, J., Haerter, J. O., & Silva, N. D. (2023). *Identification algorithm for cold pool gust fronts in weather station data from equatorial africa (version 1.0) [software & dataset].* Zenodo. Retrieved from `https://doi.org/10.5281/zenodo.10117789` doi: 10.5281/zenodo.10117789

Hunter, J. D. (2007). Matplotlib: A 2d graphics environment [software]. *Computing in Science & Engineering*, *9*(3), 90–95. doi: 10.1109/MCSE.2007.55

Jensen, G. G., Fiévet, R., & Haerter, J. O. (2021). The diurnal path to persistent convective self-aggregation. *arXiv preprint arXiv:2104.01132*.

Kirsch, B., Ament, F., & Hohenegger, C. (2021). Convective cold pools in long-term boundary layer mast observations. *Monthly Weather Review*, *149*(3), 811–820.

Kruse, I. L., Haerter, J. O., & Meyer, B. (2022). Cold pools over the netherlands: A statistical study from tower and radar observations. *Quarterly Journal of the Royal Meteorological Society*, *148*(743), 711–726.

Langhans, W., & Romps, D. M. (2015). The origin of water vapor rings in tropical oceanic cold pools. *Geophysical Research Letters*, *42*(18), 7825–7834.

Meyer, B., & Haerter, J. O. (2020, 11). Mechanical forcing of convection by cold pools: Collisions and energy scaling. *J. Adv. Model. Earth Syst.*, *12*(11), n/a–n/a. Retrieved from `https://doi.org/10.1029/2020MS002281` doi: 10.1029/2020MS002281

Mueller, C. K., & Carbone, R. E. (1987). Dynamics of a thunderstorm outflow. *Journal of the Atmospheric sciences*, *44*(15), 1879–1898.

Niehues, J., Jensen, G. G., & Haerter, J. O. (2022). Self-organized quantization and oscillations on continuous fixed-energy sandpiles. *Physical Review E*, *105*(3), 034314.

Nissen, S. B., & Haerter, J. O. (2021). Circling in on convective self-aggregation. *Journal of Geophysical Research: Atmospheres*, *126*(20), e2021JD035331.

Parker, D. J., Fink, A., Janicot, S., Ngamini, J.-B., Douglas, M., Afiesimama, E., ... others (2008). The amma radiosonde program and its implications for the future of atmospheric monitoring over africa. *Bulletin of the American Meteorological Society*, *89*(7), 1015–1028.

Purdom, J. F. (1976). Some uses of high-resolution goes imagery in the mesoscale forecasting of convection and its behavior. *Monthly Weather Review*, *104*(12), 1474–1483.

Redl, R., Fink, A. H., & Knippertz, P. (2015). An objective detection method for convective cold pool events and its application to northern africa. *Monthly Weather Review*, *143*(12), 5055–5072.

Simpson, J. (1980). Downdrafts as linkages in dynamic cumulus seeding effects. *Journal of Applied Meteorology*, *19*(4), 477–487.

TAHMO. (2023). *Trans-african hydro-meteorological observatory (tahmo) weather station data [dataset].* Retrieved from `https://tahmo.org/climate-data/`

Tompkins, A. M. (2001a). Organization of tropical convection in low vertical wind shears: The role of cold pools. *Journal of the Atmospheric Sciences*, *58*, 1650-1672. doi: 10.1175/1520-0469(2001)058<1650:ootcil>2.0.co;2

Tompkins, A. M. (2001b). Organization of tropical convection in low vertical wind shears: The role of water vapor. *Journal of the Atmospheric Sciences*, *58*(6), 529–545.

Torri, G., & Kuang, Z. (2019). On cold pool collisions in tropical boundary layers. *Geophys. Res. Lett.*, *46*, 399-407. doi: 10.1029/2018gl080501

Torri, G., Kuang, Z., & Tian, Y. (2015). Mechanisms for convection triggering by cold pools. *Geophysical Research Letters*, *42*(6), 1943–1950.

van de Giesen, N., Hut, R., & Selker, J. (2014). The trans-african hydro-meteorological observatory (tahmo). *Wiley Interdisciplinary Reviews: Water*, *1*(4), 341–348.

van den Heever, S. C., Grant, L. D., Freeman, S. W., Marinescu, P. J., Barnum, J., Bukowski, J., ... others (2021). The colorado state university convective cloud outflows and updrafts experiment (c 3 loud-ex). *Bulletin of the American Meteorological Society*, *102*(7), E1283–E1305.

Vogel, R. (2017). *The influence of precipitation and convective organization on the structure of the trades* (Unpublished doctoral dissertation). Universität Hamburg Hamburg.

Vogel, R., Konow, H., Schulz, H., & Zuidema, P. (2021). A climatology of trade-wind cumulus cold pools and their link to mesoscale cloud organization. *Atmospheric Chemistry and Physics*, *21*(21), 16609–16630.

Wakimoto, R. M. (1982). The life cycle of thunderstorm gust fronts as viewed with doppler radar and rawinsonde data. *Monthly weather review*, *110*(8), 1060–1082.

Waskom, M. L. (2021). seaborn: statistical data visualization [software]. *Journal of Open Source Software*, *6*(60), 3021. Retrieved from `https://doi.org/10.21105/joss.03021` doi: 10.21105/joss.03021

Zhang, G., Cook, K. H., & Vizy, E. K. (2016). The diurnal cycle of warm season

rainfall over west africa. part i: Observational analysis. *Journal of Climate*, *29*(23), 8423 - 8437. doi: 10.1175/JCLI-D-15-0874.1
Zipser, E. (1977). Mesoscale and convective–scale downdrafts as distinct components of squall-line structure. *Monthly Weather Review*, *105*(12), 1568–1589.
Zuidema, P., Li, Z., Hill, R. J., Bariteau, L., Rilling, B., Fairall, C., ... Hare, J. (2012). On trade wind cumulus cold pools. *Journal of the Atmospheric Sciences*, *69*(1), 258–280.
Zuidema, P., Torri, G., Muller, C., & Chandra, A. (2017). A survey of precipitation-induced atmospheric cold pools over oceans and their interactions with the larger-scale environment. *Surveys in Geophysics*, 1–23.

References From the Supporting Information

Bolton, D. (1980). The computation of equivalent potential temperature. Monthly weather review , 108 (7), 1046–1053.
Wallace, J. M., & Hobbs, P. V. (2006). Atmospheric science: an introductory survey (Vol. 92). Elsevier.

Characteristics of Station-Derived Convective Cold Pools Over Equatorial Africa

Jannik Hoeller[1,2], Jan O. Haerter[1,2,3,4], Nicolas Da Silva[1]

[1]Integrated Modeling, Leibniz Centre for Tropical Marine Research, Fahrenheitstr. 6, 28359 Bremen, Germany
[2]Niels Bohr Institute, Copenhagen University, Blegdamsvej 17, 2100 Copenhagen, Denmark
[3]Physics and Earth Sciences, Constructor University Bremen, Campus Ring 1, 28759 Bremen, Germany
[4]Department of Physics and Astronomy, University of Potsdam, Karl-Liebknecht-Straße 32, 14476 Potsdam, Germany

Key Points:

- 4289 cold pools are identified across equatorial Africa based on temperature and wind criteria.
- The occurrence and intensity of the observed cold pools are related to low-level moisture conditions and the depth of convection.
- The identified cold pool gust fronts closely correlate with satellite-observed brightness temperature discontinuities.

Corresponding author: Jannik Hoeller, `jannik.hoeller@leibniz-zmt.de`

Abstract

Due to their potential role in organizing tropical mesoscale convective systems, a better understanding of cold pool (CP) dynamics in such regions is critical, particularly over land where the diurnal cycle further concentrates convective activity. Numerical models help disentangle the processes involved but often lack observational benchmark studies. To close this gap, we analyze nearly 43 years of five-minute resolution near-surface timeseries records from twelve automatic weather stations across equatorial Africa. We identify 4289 CPs based on criteria for temperature and wind. The identified CP gust fronts, which exhibit respective median temperature and specific humidity decreases of $5.2\,K$ and $2.8\,g/kg$, closely correlate with satellite-observed brightness temperature discontinuities. Despite weak diurnal variation in precipitation, observed CP occurrence shows a pronounced diurnal cycle with an afternoon peak — a finding we attribute to low-level moisture conditions. Our findings can serve as observational benchmark to improve simulations of CP organization.

Plain Language Summary

Convective cold pools form when rain evaporates underneath thunderstorm clouds. The evaporation causes the air to cool and sink toward the ground, where it is deflected horizontally. Cold pools are thus associated with strong gusty winds, and over tropical land, they can be especially vigorous. Cold pools are also suggested to contribute to the organization of thunderstorm clouds into large clusters of rain-producing areas. The widespread, heavy rainfall can then cause flooding. To better predict such flooding in numerical weather models, having a precise observational basis for cold pool properties is essential — yet currently missing in equatorial Africa. We here provide such an observational benchmark by analyzing thousands of cold pools using timeseries of near-surface temperature, wind, humidity and precipitation. We additionally show that the cold pools can even be detected from satellite data when analyzing abrupt changes in cloud top temperature. Such satellite-based detection could open for cold pool studies across all tropical land areas — of great practical relevance to the prediction of thunderstorm clusters.

1 Introduction

Convective cold pools (CPs) are caused by the evaporation of rainfall beneath deep convective clouds (Zuidema et al., 2017). The resultant denser air volume within the subcloud layer spreads out laterally along the surface and is known to cause a so-called "gust front" along its edges. The gust front features strong horizontal and vertical winds along with moisture and temperature anomalies which together can give rise to additional deep convective events, e.g., under collisions (Purdom, 1976; Feng et al., 2015). CPs are thus important agents in mediating interactions between deep convective cells and thus the self-organization of thunderstorm systems (Simpson, 1980; Tompkins, 2001b; Haerter et al., 2019; Jensen et al., 2021).

Recent idealized cloud-resolving and large-eddy simulations have provided new quantitative and qualitative insight into CP structure and dynamics, such as scaling analysis to obtain a required mesh resolution (Fiévet et al., 2022), the potential origin of moisture rings (Langhans & Romps, 2015; Drager et al., 2020), and insight into interaction mechanisms (Tompkins, 2001a; Torri et al., 2015; Meyer & Haerter, 2020; Haerter et al., 2020). Such simulation studies have also triggered a range of simplified conceptual models, (Böing, 2016; Haerter, 2019; Haerter et al., 2019; Nissen & Haerter, 2021; Niehues et al., 2022), which may help elucidate some of the organizing mechanisms involved. New methods of CP detection in numerical studies have also been developed, which help automatize the tracking of CP gust fronts and their interactions in space and time (Gentine et al., 2016; Torri & Kuang, 2019; Fournier & Haerter, 2019; Henneberg et al., 2020; Hoeller et al., 2022; Hoeller, Fiévet, & Haerter, 2023).

Despite this progress in numerical and theoretical work, direct measurements of CPs are still limited to specific geographic regions, such as the tropical and sub-tropical ocean (Zipser, 1977; Zuidema et al., 2012; Vogel, 2017; Chandra et al., 2018; Vogel et al., 2021), and mid-latitude continental regions in Central Europe (Kirsch et al., 2021; Kruse et al., 2022) or North America (Mueller & Carbone, 1987; Wakimoto, 1982; Engerer et al., 2008; Hitchcock et al., 2019; van den Heever et al., 2021). With a focus on dust storms, in semi-arid tropical regions a CP detection method was suggested based on surface measurements and satellite microwave data (Redl et al., 2015).

The importance of collecting information on CPs and precipitation in deep tropical regions has been pointed out (Adams et al., 2015) but systematic, climatological studies on CPs in such regions are still rare or lacking. This may partially be due to difficult environmental conditions which pose challenging demands on equipment and maintenance (Parker et al., 2008). Also the availability of funds may hinder systematic long-term campaigns in some regions. A notable exception is the trans-African hydro-meteorological observatory (TAHMO) which offers a promising network of station measurements in many sub-Saharan African countries (van de Giesen et al., 2014). Using a range of stations from the TAHMO network, we here present a climatology of CP measurements for equatorial Africa and compare findings to previous work in other geographic regions.

2 Data

2.1 Station data

We utilize data from twelve ATMOS41 automatic weather stations (AWS) in equatorial Africa (Fig. 1), operated by TAHMO (TAHMO, 2023). The stations are situated in Cameroon, the Democratic Republic of the Congo (DR Congo), Nigeria, and Uganda. In order to investigate the influence of regional climatic differences on CPs, we group stations according to their respective deployment countries in the following analysis.

The AWS provide data at a temporal resolution of five minutes. All stations are installed at an approximate height of two meters above the surface. For our analysis, we employ the station records of precipitation, atmospheric pressure, air temperature, relative humidity, and wind gust speed. To derive the wind gust speed, the ATMOS41 measures the instantaneous wind speed every ten seconds and outputs the maximum instantaneous wind speed value within the corresponding five-minute interval as wind gust speed. If an instantaneous wind speed is larger than eight times the running average of the previous ten instantaneous measurements, the measurement is rejected. While this method may prevent spurious spikes in the wind record under normal conditions, it can cause missing wind data in cases of large and sudden wind changes. Given the frequent occurrence of such strong wind variations associated with CP gust fronts, approximately 22% of all identified CPs have an incomplete wind record.

We analyze the data recorded by the stations from January 1, 2019, to September 30, 2023. As not all stations were operational throughout the entire period, we limit our analysis for each station to days with complete air temperature record. Additionally, we require the air temperature to be recorded for a minimum of ten consecutive minutes from the previous day and for the subsequent 120 minutes on the following day. The resulting number of analysis days per station is indicated in Fig. 1. In total, we analyzed 15602 days and thus nearly 43 years of station data.

Based on the station-measured variables, we additionally compute both mixing ratio, r and saturated mixing ratio, r_{sat} (see Text S1), and derive the mixing ratio deficit, $r_D \equiv r_{sat} - r$ and the specific humidity, $q \equiv r/(1 + r)$.

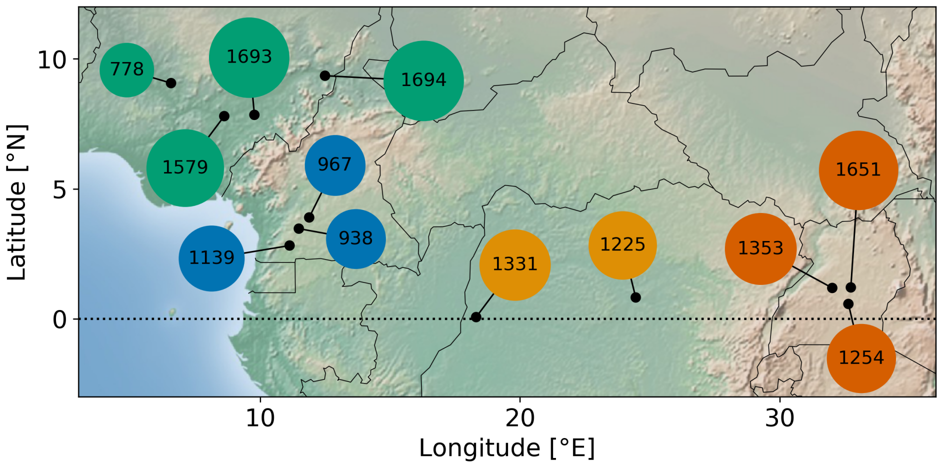

Figure 1: **Employed weather station data.** Map of equatorial Africa with station locations (filled black circles) utilized in this study. Numbers represent available days of station data with a complete record of air temperature, T. The stations are grouped into four regions denoted by the colored circles: Cameroon (blue), Democratic Republic of the Congo (yellow), Nigeria (green), Uganda (red). The area of colored circles is proportional to the available days of station data.

2.2 Satellite data

Apart from the station data, we utilize infrared brightness temperature measurements which we derive from satellite-measured effective radiances. The radiances are extracted from Meteosat Second Generation (MSG) 0° products provided by the European Organisation for the Exploitation of Meteorological Satellites (EUMETSAT) (EUMETSAT, 2023). The data has a baseline repeat cycle of $15\,min$ and a spatial resolution of $3\,km$ in the sub-satellite point. To convert the radiances to brightness temperatures we employ equation 5.3 and the corresponding regression coefficients of EUMETSAT (2012).

3 Methods

3.1 Cold Pool Detection Algorithm

(i) Temperature criterion. A potential CP event is detected at a given time t if three conditions apply: similar to Kirsch et al. (2021) we require a substantial temperature decrease $\Delta T \leq -2\,K$, within the $20\,min$ window from $t - 5\,min$ to $t + 15\,min$. Additionally, we require the decrease of ΔT to be monotonic and $T(t) - T(t - 5\,min) \leq 0.5\,K$.

(ii) Wind criterion. To verify detected potential CP events, we adapt the wind criterion introduced by Kruse et al. (2022). For this purpose, we compute the wind gust anomaly for each time t as

$$\Delta u_g(t) \equiv u_g(t) - \overline{u}_g(t)\,, \tag{1}$$

where u_g is the wind gust speed and $\overline{u}_g$ its centered 2-hour running mean, i.e., the mean value of the 25 wind gust speeds recorded during the the corresponding 2-hour window.

For a potential CP event at time t we identify the maximum wind gust anomaly, Δu_g^{max}, between $t - 20\,min$ and $t + 40\,min$. We consider it as CP event if

$$\Delta u_g^{max} \geq \overline{\Delta u}_g(t) + 3\,\sigma_{\Delta u_g}(t)\,, \tag{2}$$

with the centered 24-hour running mean of the wind gust anomaly, $\overline{\Delta u_g}$, and the corresponding 24-hour running standard deviation, $\sigma_{\Delta u_g}$.

As the CP onset is defined based on the temperature criterion, we also search for associated wind gusts in a $20\,min$ time window before CP onset. We choose $20\,min$ rather than the $10\,min$ used by Kruse et al. (2022) since our temperature criterion involves a minimum decrease of $-0.5\,K$ within $5\,min$ to define the onset of potential CPs and might thus delay the onset in comparison to Kruse et al. (2022). The $40\,min$ time window after CP onset allows significant wind offsets while ensuring a temporal relation between ΔT and Δu_g^{max}.

In case of missing wind gust anomalies between $t{-}20\,min$ and $t{+}40\,min$, we identify the maximum wind gust, u_g^{max} within this time window rather than Δu_g^{max} and consider the event a CP if

$$u_g^{max} \geq \overline{u}_g(t-80\,min) + 2\,\sigma_{u_g}(t-80\,min)\,. \tag{3}$$

By evaluating the centered 2-hour running mean $\overline{u}_g$ and the corresponding standard deviation, σ_{u_g}, $80\,min$ before CP onset, we keep again a $20\,min$ offset between CP onset and the 2-hour time window of the reference values. If no wind gust data has been recorded between $t-20\,min$ and $t+40\,min$, or if the reference values $\overline{u}_g(t-80\,min)$ and $\overline{u}_g(t{-}80\,min)$ could not be computed due to missing data, we consider the event as "no CP."

Differing from Kruse et al. (2022), we evaluate the wind criterion based on wind gust rather than wind speed. Since we work with station data with a temporal resolution of $5\,min$ in contrast to $1\,min$ in (Kruse et al., 2022), we find wind gust a better indicator for CP gust fronts than wind speed.

(iii) Duplicate detection check. Often, a CP fulfills the defined criteria (i) and (ii) not only at time t, but also at subsequent time steps. Depending on the evolution of temperature and wind gust behind the CP gust front, time steps in which the criteria are met can even be separated from each other by time steps in which the criteria are not met. In order to avoid duplicate detection of a given CP, we drop detected CP events if at least one other CP event was detected within $20\,min$ before that particular event. Given the variety of environmental conditions under which we observe CPs at our station locations, we find this definition to be more permissive than the absolute $60\,min$ time window after detected temperature decreases, within which Kirsch et al. (2021) consider any detected decrease as part of the same event.

3.2 Determination of Cold Pool Anomalies

We analyze the effects of a detected CP with respect to different station-measured meteorological variables by considering a time window relative to CP onset, t_0, from $t_0{-}40\,min$ to $t_0{+}120\,min$. Within this time window, we evaluate the CP associated anomalies $y'(t) \equiv y(t) - y_{ref}$ for a meteorological variable y based on an unperturbed reference state y_{ref}, which we define as the temporal mean of instantaneous measurements in a time interval before CP onset. Since the onset is defined based on the temperature drop and thus could be different for other variables, we choose the time interval from $t_0{-}40\,min$ to $t_0{-}20\,min$ to keep a sufficient margin of $20\,min$ to the CP onset while preserving the required temporal proximity. To minimize any distortion of the reference state through the diurnal cycle, we deviate from this definition only for temperature anomalies and follow the approach of the refined temperature drop from Kruse et al. (2022) instead, i.e., we consider the maximum temperature of the two measurements in the $10\,min$ time window preceding the CP onset as unperturbed reference temperature.

Due to the coarser temporal resolution, we extend the time window in which we analyze the anomalies before CP onset to $60\,min$ for satellite-measured $10.8\,\mu m$ brightness temperatures, $BT_{10.8}$, and define the reference brightness temperature, $BT_{10.8}^{ref}$, as the mean of the three observations in the time interval from $t_0 - 60\,min$ to $t_0 - 30\,min$. As there might not be a brightness temperature observation at the station-derived CP onset, t_0, we define the closest satellite time step as $\hat{t}_0$ and measure the CP time relative to it. The brightness temperature anomalies, $BT'_{10.8}$, are then computed analogously to those for station-measured variables. Moreover, to further investigate the space-borne CP signature, we additionally determine the temporal change of $BT'_{10.8}$, as $\Delta BT'_{10.8}(t) = BT'_{10.8}(t) - BT'_{10.8}(t - 15\,min)$.

4 Results

4.1 Seasonal and Diurnal Cycle of Observed Cold Pools

First, we derive the seasonal and diurnal cycles of CPs in the different sub-regions (Fig. 1) and relate them with precipitation, convection depth and moisture conditions (Fig. 2). With about 0.3–0.6 CPs per day in the high seasons (Fig. 2a, Table S2), equatorial Africa is a region with particular CP abundance compared to previous climatologies in other continental regions (Redl et al., 2015; Kirsch et al., 2021; Kruse et al., 2022). In every sub-region, the number of CPs peaks twice during the course of the year with a first maximum between March and May and a second maximum between September and October. The bi-modality in the annual cycle of CPs largely corresponds to the latitudinal migration of the Inter-Tropical Convergence Zone (ITCZ) which is reflected in the precipitation seasonal cycles (Fig. 2c). However, we note that precipitation may not explain all the features of the annual cycle of CPs and the differences between sub-regions. For instance, Nigeria presents a single precipitation peak in September whereas the occurrence of CPs peaks in both May and September. There, the strong CP activity during May may be related to the combination of deeper convection (Fig. 2e) fed by high equivalent potential temperatures (θ_E; Fig. S1) and of higher low-level water vapor mixing ratio deficit (r_D; Fig. 2g) boosting rain evaporation. We also note that Uganda receives the least precipitation among sub-regions while experiencing the most of CPs during the year. We attribute the larger number of CPs in Uganda to generally drier conditions at low levels (Fig. 2g).

The diurnal cycle of CPs strongly peaks between 15 LT and 18 LT in most of the regions with the exception of Nigeria where the peak is reached between 18 LT and 21 LT (Fig. 2b). The high CP activity during the afternoon can be directly related to the afternoon peak in (deep) convection, highlighted by maxima in precipitation (Fig. 2d) and lower brightness temperatures (Fig. 2f). Consistently with earlier studies (Zhang et al., 2016; Camberlin et al., 2018; Andrews et al., 2023), precipitation shows secondary nocturnal peaks in Uganda and Congo, and remains high during the night in Nigeria, whereas the proportion of CPs displays local minima during these hours. This mismatch between precipitation and CPs is likely to be related to both the decline of convection during the night (leading to weaker rainfall intensities and downdrafts) and to moister conditions at the surface (reducing rainfall evaporative cooling; Fig. 2h) which both inhibit CP formation (Zuidema et al., 2017).

4.2 Observed Cold Pool Characteristics

We further characterize equatorial African CPs by examining their related temperature and moisture anomalies (defined in Sec. 3.2). On average, a CP in equatorial Africa is accompanied by a $5\,K$ drop in temperature (compared to $3\,K$ in Germany; Kirsch et al. (2021)) occurring in about 30 minutes, with little variability among sub-regions (Fig. 3a, Table S2). Different from Kirsch et al. (2021) over Germany, we generally observe a decrease in specific humidity after the passage of CPs over equatorial Africa (Fig. 3d). Interestingly, we find that the magnitude of this decrease is smaller in the elevated (Table S1) stations of Uganda ($-1\,g/kg$) characterized by less deep convection (Fig. 2e,f)

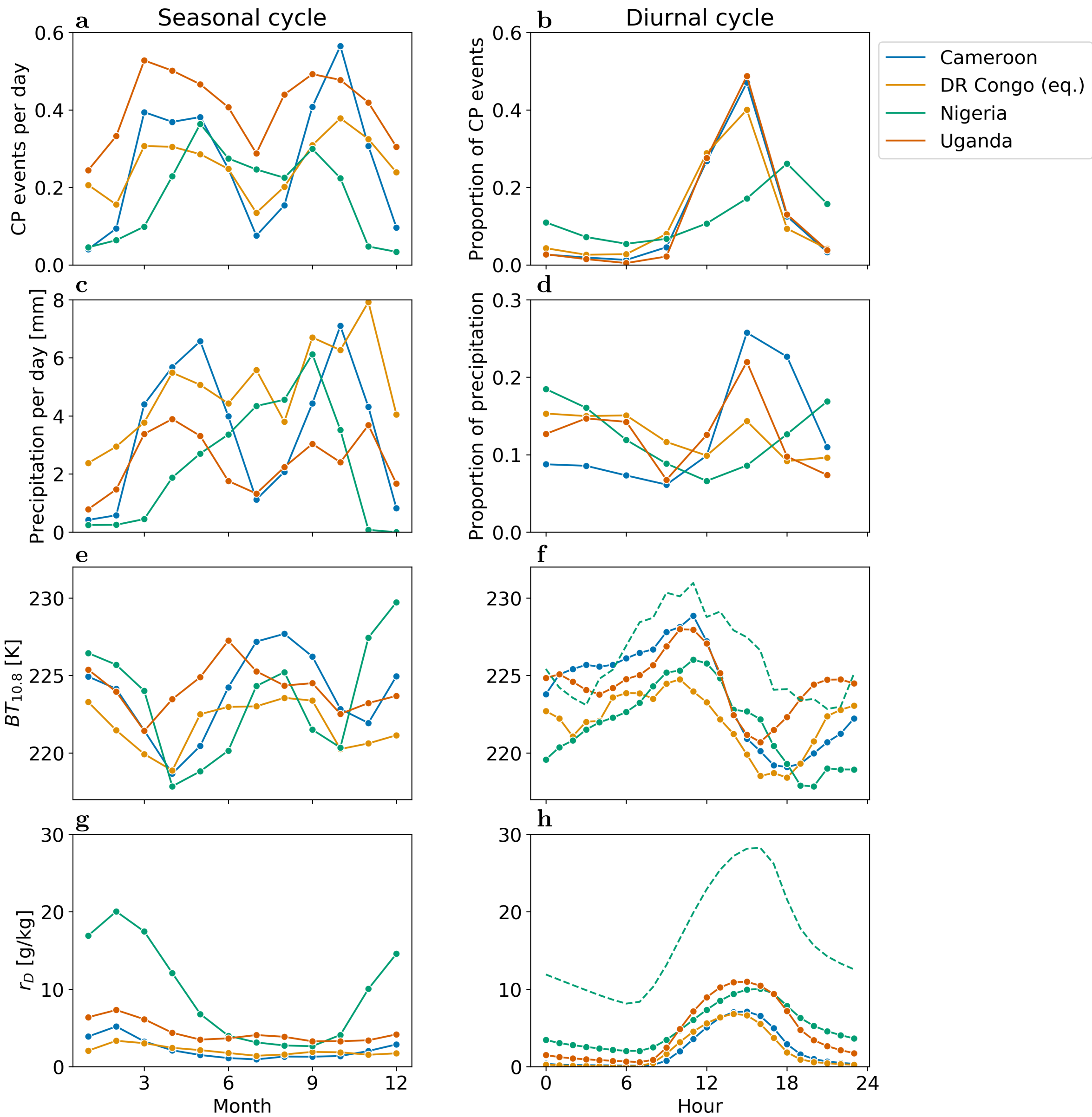

Figure 2: **Observed seasonal and diurnal cycles.** **a**, Mean number of daily cold pool (CP) events for each month. Lines interpolate linearly between markers to facilitate the interpretation; colors indicate different regions. The number of CP events is normalized based on the number of analyzed days per month and region. **b**, Proportion of CP events at different times of the day. Each marker represents the proportion of CP events observed within a given 3-hour time interval, starting with the interval [0,3) for the marker at 0 LT. Lines and colors analogous to (a). **c**, Analogous to (a) but for precipitation. **d**, Analogous to (b) but for precipitation. **e**, Mean 10.8 μm brightness temperature, $BT_{10.8}$, of deep clouds ($BT_{10.8} \leq 240\,K$) for each month. Lines and colors analogous to (a). **f**, Mean $BT_{10.8}$ of deep clouds at different times of the day. Intervals, lines and colors analogous to (b). The two lines for Nigeria represent rainy months (Apr–Oct, solid line with markers) and dry months (Nov–Mar, dashed). **g**, Analogous to (e) but for mean mixing ratio deficit, r_D. **h**, Analogous to (f) but for mean r_D.

and drier low-level environments (Fig. 2g,h) compared to the other sub-regions (about $-3\,g/kg$). Less deep convection is likely to be associated with less elevated (relative to the surface level) convective downdrafts (Zuidema et al., 2017) importing less upper-level dry air to the surface, which combined with enhanced rain evaporation due to drier environments, may explain the reduced decline in specific humidity over Uganda. When considering the 25% driest (moistest) low-level pre-CP environments, we further evidence the large impact of moisture conditions, and thus of rain evaporation, on CP temperature and moisture anomalies in all sub-regions (Fig. 2b,c,e,f). Indeed, we find CP anomalies that are on average $3\,K$ cooler and $2\,g/kg$ moister in the driest pre-CP conditions than in the moistest pre-CP conditions. We note weak maxima in specific humidity occurring few minutes after the CP onset (so-called moisture rings) over Cameroon, Uganda and Congo for the driest pre-CP environments. Finally, the temporal evolutions of r_D (Fig. 3g,h,i) reveal that in the driest environments, rain evaporation is not sufficient to saturate the low-level air (similar to Germany; Kirsch et al. (2021)).

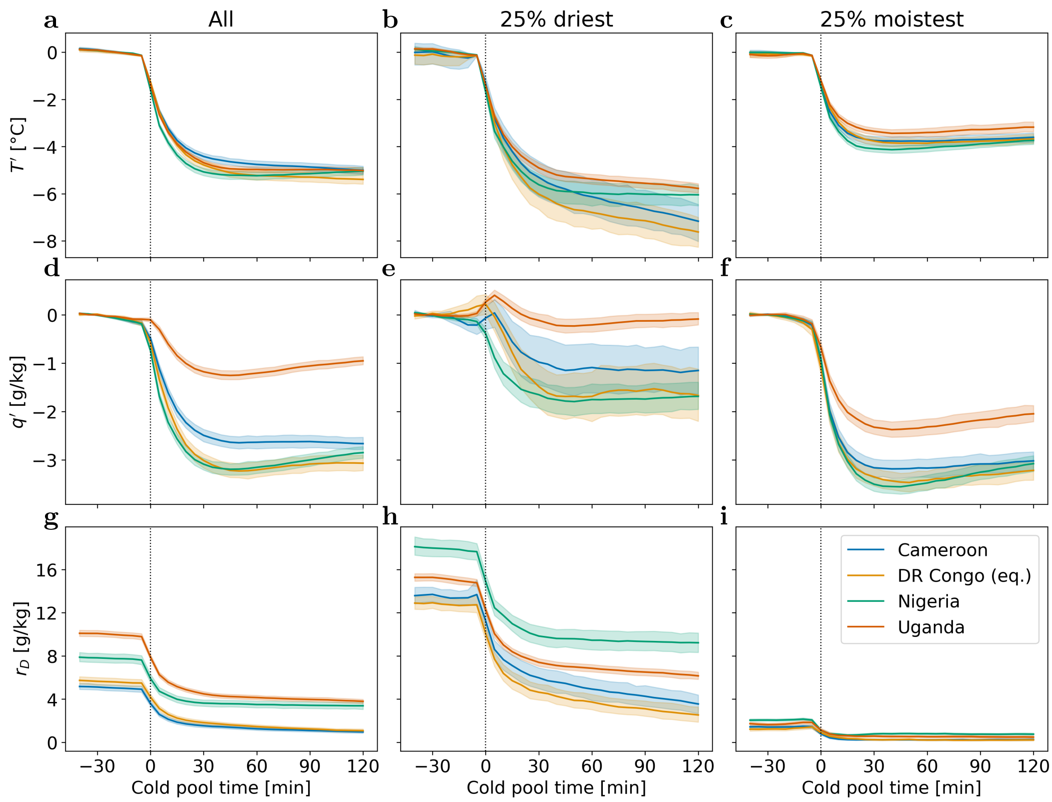

Figure 3: **Station-derived cold pool (CP) properties relative to CP onset, t_0.** **a**, Mean temperature anomalies, T', for different regions; shading indicates the 95% confidence interval. **b**, Analogous to (a) but for the 25% driest CPs of each region w.r.t. the reference mixing ratio deficit, r_D^{ref}, prior to t_0. **c**, Analogous to (b) but for the 25% moistest CPs. **d**–**f**, Analogous to (a)–(c) but for mean specific humidity anomalies, q'. **g**–**i**, Analogous to (a)–(c) but for mean mixing ratio deficits, r_D. Note that only timeseries of CPs, where t_0 is more than 120 minutes apart from other CP onsets, are included in the analysis.

Moving to CP cloud characteristics, we find that 92% (Nigeria) to 100% (Congo) of CP gust fronts are accompanied by shallow or deep convective clouds (Fig. S2a). More specifically, a CP is generally accompanied by a strong (reaching $30\,K$ in Cameroon) decrease in $BT_{10.8}$ (Fig. 4a). The $BT_{10.8}$ minimum is typically reached 30–45 minutes after CP onset. While this minimum is delayed w.r.t. the CP onset, we find a minimum of the time derivative of $BT'_{10.8}$ synchronized with the CP onset in all sub-regions (Fig. 4b). This observation suggests that CPs in equatorial Africa, and potentially other regions, might be detectable from space-borne satellite data.

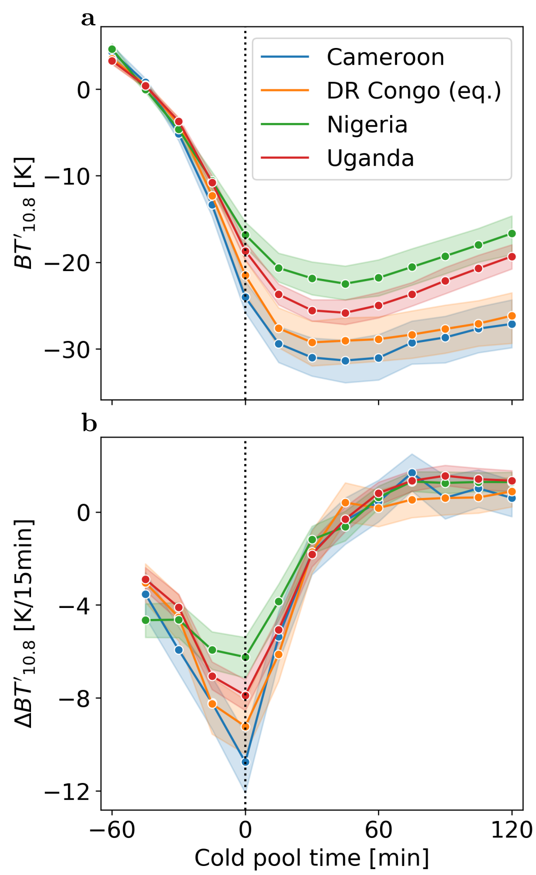

Figure 4: **Space-borne signatures of cold pools (CPs) relative to CP onset, $\hat{t}_0$.** **a**, Mean 10.8μm brightness temperature anomalies, $BT'_{10.8}$, of station-derived CPs for different regions; shading indicates the 95% confidence interval. **b**, Analogous to (a) but for the corresponding derivative $\Delta BT'_{10.8}$.

4.3 Cold Pool Examples With Deep and Shallow Convection

We now turn to two contrasting examples of observed CPs (Fig. 5). The two station locations at which the CPs were detected are indicated in Fig. 5a).

The first CP (Fig. 5; left column) was detected in DR Congo at station TA673 on November 28, 2021, at 13:40 UTC. The CP was associated with a mesoscale convective system, visible in the satellite-derived 10.8 μm brightness temperature image at 13:45 UTC (Fig. 5b). The corresponding brightness temperature timeseries of different satellite channels at the station are depicted in Fig. 5d). All channels show a significant brightness temperature decrease around CP onset, with a maximum decrease rate right at the onset. Between 12:30 and 14:45 UTC, the brightness temperature dropped by 85 K in the 10.8 μm channel and then slowly increased again. The station record (Fig. 5f) further reveals a massive air temperature drop of 9.6 K between 13:40 and 14:00 UTC, accompanied by increased wind gust speeds of up to 6.5 m/s. By 14:00 UTC, when the temperature stabilized again, the air became fully saturated. Five minutes later, the rainfall intensity peaked at approximately $65\,mm/h$.

The second CP (Fig. 5; right column) was detected in Uganda at station TA222 on July 2, 2021, at 12:05 UTC. During the time it was detected, the CP featured arc-shaped shallow convection at the gust front, distinctly separated from the parent convection by clear skies (Fig. 5c). The corresponding brightness temperature timeseries at the station (Fig. 5e) confirm the passage of low-level clouds right at the time of the station-derived CP onset. Around the CP onset, no rainfall was measured at the station (Fig. 5g). This time, the observed wind gust speeds increase approximately 5–10 minutes before the drop in air temperature and reach a peak value of $10\,m/s$ at CP onset.

5 Summary and Discussion

The present study provides multi-year statistics of cold pool characteristics in equatorial Africa, based on five-minute near-surface weather data. Using detection methods similar to those in previous studies focused on mid-latitude continental regions, key findings include that temperature drops upon gust front passage often exceed $5\,K$ and specific humidities typically decrease by more than $3\,g/kg$. Weak moisture rings can only be identified for the driest cold pools in some of the regions — in agreement with Kruse et al. (2022) for data in the Netherlands where moisture rings were generally not detected.

Seasonally, the rate of cold pool occurrence roughly follows precipitation statistics. Yet, diurnally, the fact that the nocturnal boundary layer is often close to saturation may focus the diurnal cycle of cold pool occurrence on the drier late afternoon times. This may have important implications for thunderstorm organization through cold pool activity: the limited time window where cold pools actually occur during the day means that self-organization may be limited to relatively short periods of the day. One could speculate that it is the lack of cold pool activity that limits the duration of mesoscale convective systems, often less than 12 hours, rather than the precipitation itself (which is more spread out over the day). Future studies should analyze if deep convection is more scattered during the nocturnal periods when fewer cold pools occur. Comparisons with oceanic cold pools and their organizational effects, which tend to be weaker (Zuidema et al., 2017), would be useful.

Our cold pool detection algorithm can be adapted to other regions, provided that there are in-situ weather stations measuring surface wind and temperature with at least a 5-minute temporal resolution. However, in-situ weather stations meeting this requirement are still limited in the tropics, whereas cold pools are abundant. Encouragingly, our findings may have implications for satellite-based cold pool detection: we show that the gust front passage clearly correlates with discontinuities in satellite-derived brightness temperature. We generally observe a significant decrease in brightness temperatures around the time of the gust front passage, with maximum decrease rates at the station-derived cold pool onset. Our findings thus suggest that cold pools in equatorial Africa, and potentially other regions, could be directly detectable from geostationary satellite data on a continental scale. Even in cases where not all parts of a cold pool gust front exhibit brightness temperature drops (Fig. S2b), neural networks, such as those developed by Hoeller, Fiévet, and Haerter (2023), may still possess the capability to detect the overall two-dimensional pattern and accurately track the gust front.

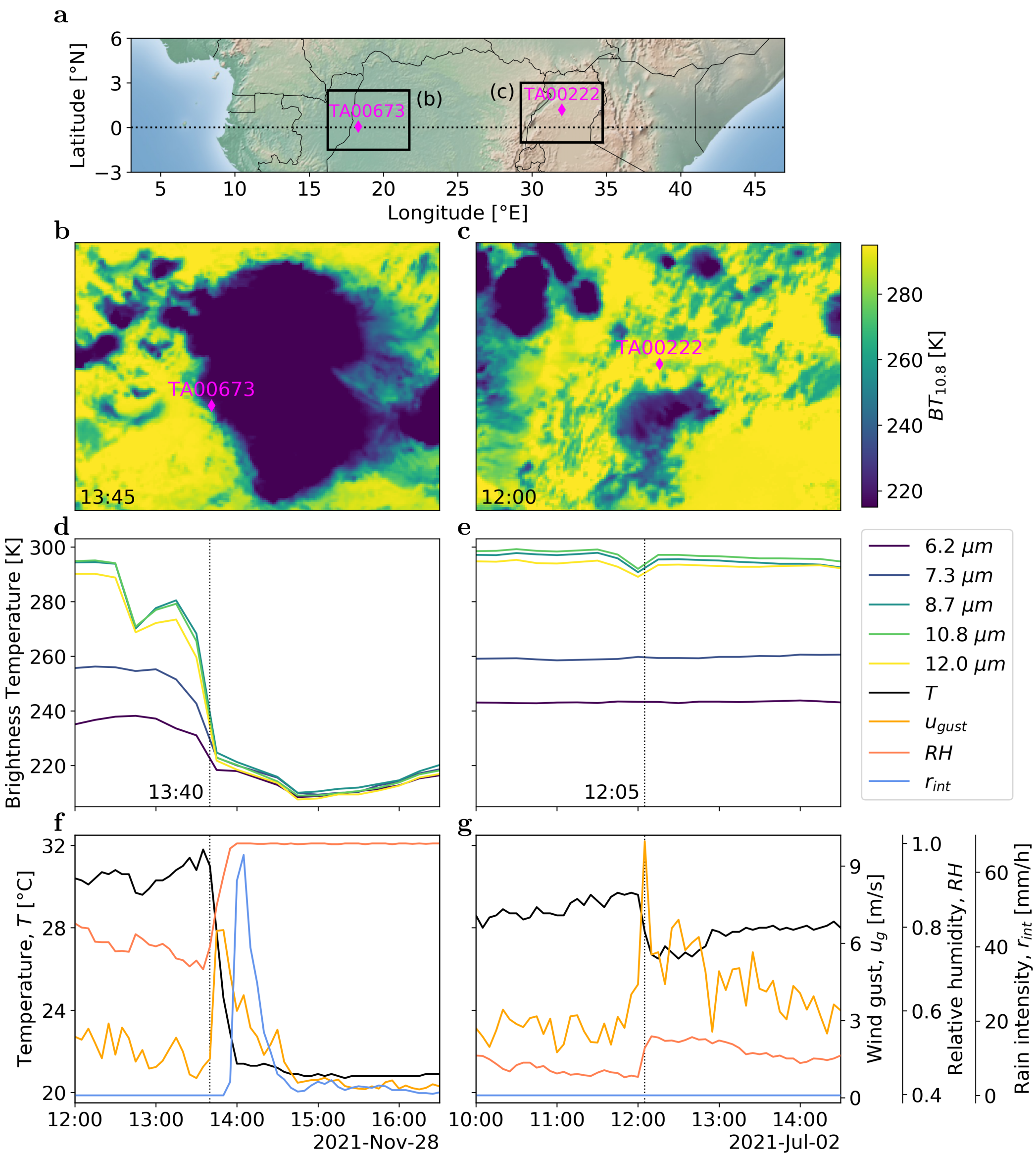

Figure 5: **Cold pool (CP) case studies.** **a**, Map displaying the locations of the stations utilized in the two case studies. Rectangles indicate the regions depicted in (b) and (c). **b**, Satellite-derived $10.8\mu m$ brightness temperatures, $BT_{10.8}$, in the vicinity of station TA00673 on November 28, 2021, at 13:45, close to a station-derived CP onset at 13:40. **c**, Analogous to (b) but for station TA00222 on July 2, 2021, at 12:00 and a CP onset at 12:05. **d**, Timeseries of satellite-derived brightness temperatures at station TA673 during the CP event visualized in (b). **e**, Analogous to (d) but for the CP event at station TA222 visualized in (c). **f-g**, Analogous to (d-e) but for different near-surface observations.

Data Availability Statement

Both the code for the cold pool gust front identification and the processed data sets are licensed under Creative Commons Attribution 4.0 International and were used in version 1.0 (Hoeller, Haerter, & Silva, 2023). The raw data of the automatic weather stations was provided by TAHMO (TAHMO, 2023) and is not publicly available. Interested parties may contact info@tahmo.org for this data. The satellite-observed radiances were extracted from Meteosat Second Generation (MSG) 0° products, provided by EUMETSAT without a licence on an unrestricted basis (EUMETSAT, 2023). Figures were made with Matplotlib version 3.5.2 (Hunter, 2007; Caswell et al., 2022) and seaborn version 0.12.2 (Waskom, 2021).

Conflicts of Interest Statement

The authors have no conflicts of interest to declare.

Acknowledgments
The authors gratefully acknowledge funding by a grant from the VILLUM Foundation (grant number: 13168) and the European Research Council (ERC) under the European Union's Horizon 2020 research and innovation program (grant number: 771859) and the Novo Nordisk Foundation Interdisciplinary Synergy Program (grant no. NNF19OC0057374). This work used resources of the Deutsches Klimarechenzentrum (DKRZ), granted by its Scientific Steering Committee (WLA) under project ID bb1166. Additionally, the authors thank the Trans-African Hydro-Meteorological Observatory (TAHMO) for the provision of meteorological data. Interested parties may contact info@tahmo.org for these data.

References

Adams, D. K., Fernandes, R. M., Holub, K. L., Gutman, S. I., Barbosa, H. M., Machado, L. A., ... others (2015). The amazon dense gnss meteorological network: A new approach for examining water vapor and deep convection interactions in the tropics. *Bulletin of the American Meteorological Society*, *96*(12), 2151–2165.

Andrews, P. C., Cook, K. H., & Vizy, E. K. (2023). Mesoscale convective systems in the congo basin: seasonality, regionality, and diurnal cycles. *Climate Dynamics*, 1–22. doi: 10.1007/s00382-023-06903-7

Böing, S. J. (2016). An object-based model for convective cold pool dynamics. *Mathematics of Climate and Weather Forecasting*, *2*(1).

Camberlin, P., Gitau, W., Planchon, O., Dubreuil, V., Funatsu, B. M., & Philippon, N. (2018). Major role of water bodies on diurnal precipitation regimes in eastern africa. *International Journal of Climatology*, *38*(2), 613-629. Retrieved from `https://rmets.onlinelibrary.wiley.com/doi/abs/10.1002/joc.5197` doi: https://doi.org/10.1002/joc.5197

Caswell, T. A., Droettboom, M., Lee, A., de Andrade, E. S., Hoffmann, T., Klymak, J., ... Ivanov, P. (2022). *matplotlib/matplotlib: Release (version 3.5.2) [software].* Zenodo. Retrieved from `https://doi.org/10.5281/zenodo.6513224` doi: 10.5281/zenodo.6513224

Chandra, A. S., Zuidema, P., Krueger, S., Kochanski, A., de Szoeke, S. P., & Zhang, J. (2018). Moisture distributions in tropical cold pools from equatorial indian ocean observations and cloud-resolving simulations. *Journal of Geophysical Research: Atmospheres*, *123*(20), 11–445.

Drager, A. J., Grant, L. D., & van den Heever, S. C. (2020). Cold pool responses to changes in soil moisture. *Journal of Advances in Modeling Earth Systems*, *12*(8), e2019MS001922.

Engerer, N. A., Stensrud, D. J., & Coniglio, M. C. (2008). Surface characteristics of observed cold pools. *Monthly Weather Review*, *136*(12), 4839–4849.

EUMETSAT. (2012). *The conversion from effective radiances to equivalent brightness temperatures (version 1).* Retrieved from `https://www-cdn.eumetsat.int/files/2020-04/pdf_effect_rad_to_brightness.pdf`

EUMETSAT. (2023). *Meteosat second generation (msg) high rate seviri level 1.5 image data - 0 degree [dataset].* Retrieved from `https://navigator.eumetsat.int/product/EO:EUM:DAT:MSG:HRSEVIRI`

Feng, Z., Hagos, S., Rowe, A. K., Burleyson, C. D., Martini, M. N., & de Szoeke, S. P. (2015). Mechanisms of convective cloud organization by cold pools over tropical warm ocean during the amie/dynamo field campaign. *Journal of Advances in Modeling Earth Systems*, *7*(2), 357–381.

Fiévet, R., Meyer, B., & Haerter, J. O. (2022). On the sensitivity of convective cold pools to mesh resolution. *Earth and Space Science Open Archive*, 24. Retrieved from `https://doi.org/10.1002/essoar.10512297.1` doi: 10.1002/essoar.10512297.1

Fournier, M. B., & Haerter, J. O. (2019). Tracking the gust fronts of convective cold pools. *Journal of Geophysical Research: Atmospheres*, *124*(21), 11103–11117.

Gentine, P., Garelli, A., Park, S., Nie, J., Torri, G., & Kuang, Z. (2016). Role of surface heat fluxes underneath cold pools. *Geophys. Res. Lett.*, *43*, 874-883. doi: 10.1002/2015gl067262

Haerter, J. O. (2019). Convective self-aggregation as a cold pool-driven critical phenomenon. *Geophysical Research Letters*, *46*(7), 4017–4028. doi: https://doi.org/10.1029/2018GL081817

Haerter, J. O., Böing, S. J., Henneberg, O., & Nissen, S. B. (2019). Circling in on convective organization. *Geophysical Research Letters*, *46*(12), 7024–7034. doi: https://doi.org/10.1029/2019GL082092

Haerter, J. O., Meyer, B., & Nissen, S. B. (2020). Diurnal self-aggregation. *npj Climate and Atmospheric Science*, *3*. doi: 10.1038/s41612-020-00132-z

Henneberg, O., Meyer, B., & Haerter, J. O. (2020). Particle-based tracking of cold pool gust fronts. *J. Adv. Model. Earth Syst.*, *12*. doi: 10.1029/2019ms001910

Hitchcock, S. M., Schumacher, R. S., Herman, G. R., Coniglio, M. C., Parker, M. D., & Ziegler, C. L. (2019). Evolution of pre-and postconvective environmental profiles from mesoscale convective systems during pecan. *Monthly Weather Review*, *147*(7), 2329–2354.

Hoeller, J., Fiévet, R., & Haerter, J. O. (2022). U-net segmentation for the detection of convective cold pools from cloud and rainfall fields. *Authorea Preprints*.

Hoeller, J., Fiévet, R., & Haerter, J. O. (2023). Detecting cold pool family trees in convection resolving simulations. *Authorea Preprints*.

Hoeller, J., Haerter, J. O., & Silva, N. D. (2023). *Identification algorithm for cold pool gust fronts in weather station data from equatorial africa (version 1.0) [software & dataset].* Zenodo. Retrieved from `https://doi.org/10.5281/zenodo.10117789` doi: 10.5281/zenodo.10117789

Hunter, J. D. (2007). Matplotlib: A 2d graphics environment [software]. *Computing in Science & Engineering*, *9*(3), 90–95. doi: 10.1109/MCSE.2007.55

Jensen, G. G., Fiévet, R., & Haerter, J. O. (2021). The diurnal path to persistent convective self-aggregation. *arXiv preprint arXiv:2104.01132*.

Kirsch, B., Ament, F., & Hohenegger, C. (2021). Convective cold pools in long-term boundary layer mast observations. *Monthly Weather Review*, *149*(3), 811–820.

Kruse, I. L., Haerter, J. O., & Meyer, B. (2022). Cold pools over the netherlands: A statistical study from tower and radar observations. *Quarterly Journal of the Royal Meteorological Society*, *148*(743), 711–726.

Langhans, W., & Romps, D. M. (2015). The origin of water vapor rings in tropical oceanic cold pools. *Geophysical Research Letters*, *42*(18), 7825–7834.

Meyer, B., & Haerter, J. O. (2020, 11). Mechanical forcing of convection by cold pools: Collisions and energy scaling. *J. Adv. Model. Earth Syst.*, *12*(11), n/a–n/a. Retrieved from https://doi.org/10.1029/2020MS002281 doi: 10.1029/2020MS002281

Mueller, C. K., & Carbone, R. E. (1987). Dynamics of a thunderstorm outflow. *Journal of the Atmospheric sciences*, *44*(15), 1879–1898.

Niehues, J., Jensen, G. G., & Haerter, J. O. (2022). Self-organized quantization and oscillations on continuous fixed-energy sandpiles. *Physical Review E*, *105*(3), 034314.

Nissen, S. B., & Haerter, J. O. (2021). Circling in on convective self-aggregation. *Journal of Geophysical Research: Atmospheres*, *126*(20), e2021JD035331.

Parker, D. J., Fink, A., Janicot, S., Ngamini, J.-B., Douglas, M., Afiesimama, E., ... others (2008). The amma radiosonde program and its implications for the future of atmospheric monitoring over africa. *Bulletin of the American Meteorological Society*, *89*(7), 1015–1028.

Purdom, J. F. (1976). Some uses of high-resolution goes imagery in the mesoscale forecasting of convection and its behavior. *Monthly Weather Review*, *104*(12), 1474–1483.

Redl, R., Fink, A. H., & Knippertz, P. (2015). An objective detection method for convective cold pool events and its application to northern africa. *Monthly Weather Review*, *143*(12), 5055–5072.

Simpson, J. (1980). Downdrafts as linkages in dynamic cumulus seeding effects. *Journal of Applied Meteorology*, *19*(4), 477–487.

TAHMO. (2023). *Trans-african hydro-meteorological observatory (tahmo) weather station data [dataset].* Retrieved from https://tahmo.org/climate-data/

Tompkins, A. M. (2001a). Organization of tropical convection in low vertical wind shears: The role of cold pools. *Journal of the Atmospheric Sciences*, *58*, 1650-1672. doi: 10.1175/1520-0469(2001)058<1650:ootcil>2.0.co;2

Tompkins, A. M. (2001b). Organization of tropical convection in low vertical wind shears: The role of water vapor. *Journal of the Atmospheric Sciences*, *58*(6), 529–545.

Torri, G., & Kuang, Z. (2019). On cold pool collisions in tropical boundary layers. *Geophys. Res. Lett.*, *46*, 399-407. doi: 10.1029/2018gl080501

Torri, G., Kuang, Z., & Tian, Y. (2015). Mechanisms for convection triggering by cold pools. *Geophysical Research Letters*, *42*(6), 1943–1950.

van de Giesen, N., Hut, R., & Selker, J. (2014). The trans-african hydro-meteorological observatory (tahmo). *Wiley Interdisciplinary Reviews: Water*, *1*(4), 341–348.

van den Heever, S. C., Grant, L. D., Freeman, S. W., Marinescu, P. J., Barnum, J., Bukowski, J., ... others (2021). The colorado state university convective cloud outflows and updrafts experiment (c 3 loud-ex). *Bulletin of the American Meteorological Society*, *102*(7), E1283–E1305.

Vogel, R. (2017). *The influence of precipitation and convective organization on the structure of the trades* (Unpublished doctoral dissertation). Universität Hamburg Hamburg.

Vogel, R., Konow, H., Schulz, H., & Zuidema, P. (2021). A climatology of trade-wind cumulus cold pools and their link to mesoscale cloud organization. *Atmospheric Chemistry and Physics*, *21*(21), 16609–16630.

Wakimoto, R. M. (1982). The life cycle of thunderstorm gust fronts as viewed with doppler radar and rawinsonde data. *Monthly weather review*, *110*(8), 1060–1082.

Waskom, M. L. (2021). seaborn: statistical data visualization [software]. *Journal of Open Source Software*, *6*(60), 3021. Retrieved from https://doi.org/10.21105/joss.03021 doi: 10.21105/joss.03021

Zhang, G., Cook, K. H., & Vizy, E. K. (2016). The diurnal cycle of warm season rainfall over west africa. part i: Observational analysis. *Journal of Climate*, *29*(23), 8423 - 8437. doi: 10.1175/JCLI-D-15-0874.1

Zipser, E. (1977). Mesoscale and convective–scale downdrafts as distinct components of squall-line structure. *Monthly Weather Review*, *105*(12), 1568–1589.

Zuidema, P., Li, Z., Hill, R. J., Bariteau, L., Rilling, B., Fairall, C., . . . Hare, J. (2012). On trade wind cumulus cold pools. *Journal of the Atmospheric Sciences*, *69*(1), 258–280.

Zuidema, P., Torri, G., Muller, C., & Chandra, A. (2017). A survey of precipitation-induced atmospheric cold pools over oceans and their interactions with the larger-scale environment. *Surveys in Geophysics*, 1–23.

References From the Supporting Information

Bolton, D. (1980). The computation of equivalent potential temperature. Monthly weather review , 108 (7), 1046–1053.

Wallace, J. M., & Hobbs, P. V. (2006). Atmospheric science: an introductory survey (Vol. 92). Elsevier.

Supporting Information for "Characteristics of Station-Derived Convective Cold Pools Over Equatorial Africa"

Jannik Hoeller[1,2], Jan O. Haerter[1,2,3,4], Nicolas Da Silva[1]

[1]Integrated Modeling, Leibniz Centre for Tropical Marine Research, Fahrenheitstr. 6, 28359 Bremen, Germany

[2]Niels Bohr Institute, Copenhagen University, Blegdamsvej 17, 2100 Copenhagen, Denmark

[3]Physics and Earth Sciences, Constructor University Bremen, Campus Ring 1, 28759 Bremen, Germany

[4]Department of Physics and Astronomy, University of Potsdam, Karl-Liebknecht-Straße 32, 14476 Potsdam, Germany

Contents of this file

1. Text S1
2. Tables S1 to S2
3. Figures S1 to S2

Introduction

Text S1 describes the computation employed for mixing ratio, saturated mixing ratio, equivalent potential temperature, and temperature at the lifting condensation level. Table S1 presents geographic information regarding the deployed automatic weather stations. Table S2 summarizes statistics on the 4289 cold pools (CPs) which we identified in five-minute near-surface data of twelve automatic weather stations in tropical Africa, recorded between January 1, 2019 and September 30, 2023. Fig. S1 shows the station-derived seasonal and diurnal cycle of near-surface equivalent potential temperature for different regions across equatorial Africa. Fig. S2 shows two probability distributions of satellite-derived properties of the identified cold pool gust fronts.

As in the main article, the statistics in Table S2, as well as the data in Fig. S1 and Fig. S2, are grouped based on the stations' deployment countries to enable an investigation of regional differences. In addition to general information on CP occurrence, Table S2 contains data on the strength of station-observed near-surface CP anomalies, as well as satellite-observed brightness temperatures. We assess the overall strength of a an anomaly by its largest extreme value in the time window from $t_0 - 20\,min$ to $t_0 + 120\,min$. Only for temperature, T, based on which the CP onset was defined, we consider the time window from t_0 to $t_0 + 120\,min$ instead. For simplicity we refer to extreme values of anomalies as perturbations and denote them with a "δ". Whether the identified extreme values are maxima or minima depends on the variable and the detected CP: While we exclusively search for minima for T and equivalent potential temperature (θ_e), we look for maxima for wind gust speed (u_g), relative humidity (RH) and atmospheric pressure (p). For specific humidity, q, which may exhibit positive as well as negative perturbations, we search for both minima and maxima and consider the extreme value with the larger absolute value as perturbation. We define a maximum or minimum, respectively, as the largest local maximum or minimum in the corresponding time window. An instantaneous measurement $y(t)$ at time t is a local maximum if $y(t - 5\,min) \leq y(t) > y(t + 5\,min)$

and analogously for a local minimum. If a certain anomaly record of an identified CP has missing values or does not have an extreme value, we do not assign a perturbation. With respect to satellite-observed brightness temperatures, we evaluate the minimum brightness temperature, $BT_{10.8}^{min}$ by determining the minimum $10.8\,\mu m$ brightness temperature in the time window from $\hat{t}_0 - 60\,min$ to $\hat{t}_0 + 120\,min$, i.e., the corresponding time window around the satellite-observed CP onset, $\hat{t}_0$, which we define in the main article.

Text S1.

Based on the station-measured variables, we compute the saturated vapor pressure of water, e_{sat}, using equation 10 of Bolton (1980). We then derive the saturated mixing ratio, r_{sat}, by plugging e_{sat} and the station-measured atmospheric pressure, p, into the following equation from chapter 3.5.1 of Wallace and Hobbs (2006):

$$r_{sat} = 0.622 \frac{e_{sat}}{p - e_{sat}}. \tag{1}$$

To compute the mixing ratio, r, we adapt equation 3.64 of Wallace and Hobbs (2006). For the computation of the temperature at the lifting condensation level, T_{LCL}, and the equivalent potential temperature, θ_E, we employ equation 22 and 43, respectively, of Bolton (1980).

References

Bolton, D. (1980). The computation of equivalent potential temperature. *Monthly weather review*, *108*(7), 1046–1053.

Wallace, J. M., & Hobbs, P. V. (2006). *Atmospheric science: an introductory survey* (Vol. 92). Elsevier.

Table S1. Geographic information regarding the deployed automatic weather stations.

Station code	Country	Latitude [°N]	Longitude [°E]	Elevation [m]
TA00220	Uganda	1.21	32.74	1047
TA00222	Uganda	1.19	32.02	1069
TA00224	Uganda	0.57	32.64	1168
TA00410	DR Congo	0.82	24.46	464
TA00459	Nigeria	9.07	6.57	198
TA00580	Nigeria	7.84	9.78	162
TA00581	Nigeria	9.35	12.50	220
TA00584	Nigeria	7.80	8.62	104
TA00673	DR Congo	0.07	18.31	311
TA00717	Cameroon	3.90	11.89	734
TA00728	Cameroon	2.82	11.13	581
TA00730	Cameroon	3.47	11.49	665

Table S2. Summary of observed cold pool (CP) statistics including the total number of CPs and CPs per day, along with median values of different CP properties; sub- and superscripts indicate the interquartile range.

	Cameroon	DR Congo (eq.)	Nigeria	Uganda	All
$\#CPs$	791	652	1086	1760	4289
$\#CPs/day$	0.26	0.26	0.19	0.41	0.24
δT	$-4.90^{+1.20}_{-1.70}$	$-5.50^{+1.60}_{-1.80}$	$-5.30^{+1.40}_{-2.00}$	$-5.30^{+1.50}_{-2.00}$	$-5.20^{+1.40}_{-2.00}$
δq	$-3.06^{+1.07}_{-1.14}$	$-3.70^{+1.03}_{-1.23}$	$-3.68^{+1.30}_{-1.13}$	$-1.91^{+1.3}_{-0.95}$	$-2.80^{+1.31}_{-1.27}$
δu_g	$2.84^{+1.28}_{-0.99}$	$2.83^{+1.43}_{-1.00}$	$4.25^{+1.91}_{-1.69}$	$3.18^{+1.25}_{-0.90}$	$3.18^{+1.39}_{-1.04}$
$\delta \theta_e$	$-15.92^{+4.30}_{-5.09}$	$-18.45^{+4.57}_{-6.43}$	$-17.94^{+5.25}_{-5.66}$	$-12.51^{+4.50}_{-4.60}$	$-15.37^{+4.98}_{-5.48}$
δRH	$0.15^{+0.07}_{-0.07}$	$0.16^{+0.07}_{-0.08}$	$0.13^{+0.08}_{-0.05}$	$0.21^{+0.08}_{-0.07}$	$0.17^{+0.07}_{-0.07}$
δp	$1.23^{+0.77}_{-0.67}$	$1.35^{+0.75}_{-0.77}$	$1.65^{+0.83}_{-0.73}$	$0.85^{+0.60}_{-0.45}$	$1.18^{+0.75}_{-0.63}$
$BT_{10.8}^{min}$	212^{+22}_{-11}	208^{+23}_{-11}	206^{+27}_{-10}	222^{+30}_{-15}	214^{+30}_{-12}

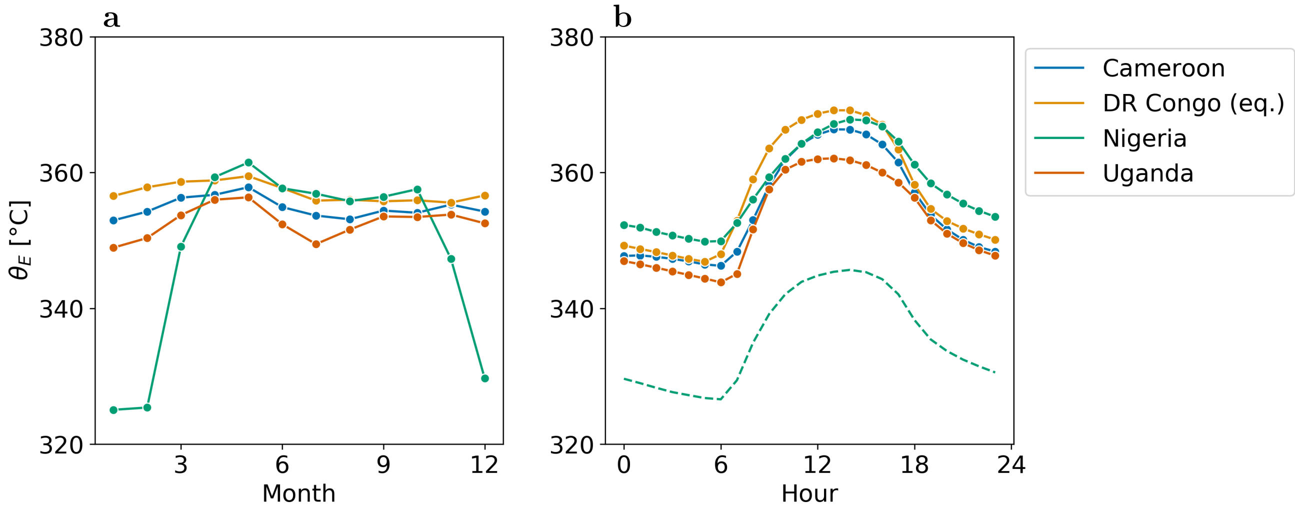

Figure S1. Station-derived seasonal and diurnal cycle of near-surface equivalent potential temperature, θ_E. **a**, Mean θ_E for each month. Lines interpolate linearly between markers to facilitate the interpretation; colors indicate different regions. **b**, Mean θ_E at different times of the day. Each marker represents the mean value for a given 3-hour time interval, starting with the interval [0,3) for the marker at 0 LT. Lines and colors analogous to (a). The two lines for Nigeria represent rainy months (Apr–Oct, solid line with markers) and dry months (Nov–Mar, dashed).

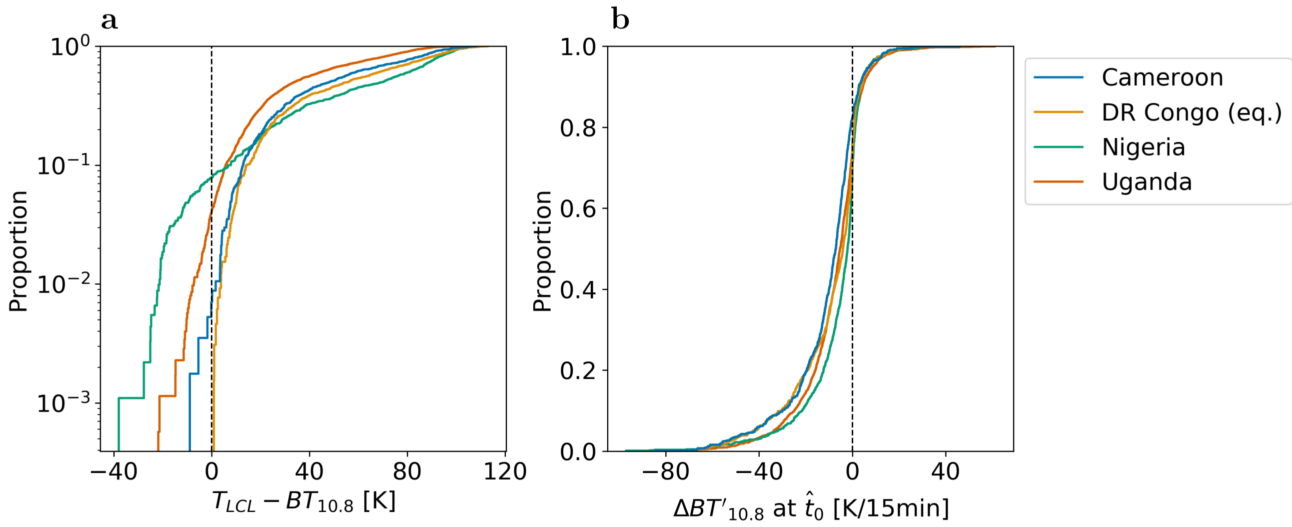

Figure S2. Probability distributions of satellite-derived cold pool (CP) properties. **a**, Distribution of the difference between the temperature at the lifting condensation level, T_LCL, and the corresponding 10.8 μm brightness temperature, $BT_{10.8}$ of identified CP gust fronts; to increase the robustness, the difference is calculated based on the mean values of the two measurements at the nearest satellite time steps around the station-derived CP onset, t_0. Values below zero represent gust fronts with clear skies. Colors indicate different regions. **b**, Distribution of the temporal change of 10.8 μm brightness temperature anomalies, $\Delta BT'_{10.8}$, at the satellite-observed CP onset, $\hat{t}_0$; colors analogous to (a).